

ARTICLE TYPE

Measuring the global 21-cm signal with the MWA-II: improved characterisation of lunar-reflected radio frequency interference

Himanshu Tiwari,^{1,2} Benjamin McKinley,^{1,3} Cathryn M. Trott,^{1,3} and Nithyanandan Thyagarajan²¹International Centre for Radio Astronomy Research (ICRAR), Curtin University, Kent Street, Bentley, Perth, Western Australia, 6102.²Commonwealth Scientific and Industrial Research Organisation (CSIRO), Space & Astronomy, P. O. Box 1130, Bentley, WA 6102, Australia.³ARC Centre of Excellence for All Sky Astrophysics in Three Dimensions (ASTRO-3D), Australia.**Author for correspondence:** Himanshu Tiwari, Email: himanshu.tiwari@postgrad.curtin.edu.au.**Abstract**

Radio interferometers can potentially detect the sky-averaged signal from the Cosmic Dawn (CD) and the Epoch of Reionisation (EoR) by studying the Moon as a thermal block to the foreground sky. The first step is to mitigate the Earth-based RFI reflections (Earthshine) from the Moon, which significantly contaminate the FM band $\approx 88 - 110$ MHz, crucial to CD-EoR science. We analysed MWA phase-I data from 72–180 MHz at 40 kHz resolution to understand the nature of Earthshine over three observing nights. We took two approaches to correct the Earthshine component from the Moon. In the first method, we mitigated the Earthshine using the flux density of the two components from the data, while in the second method, we used simulated flux density based on an FM catalogue to mitigate the Earthshine. Using these methods, we were able to recover the expected Galactic foreground temperature of the patch of sky obscured by the Moon. We performed a joint analysis of the Galactic foregrounds and the Moon's intrinsic temperature (T_{Moon}) while assuming that the Moon has a constant thermal temperature throughout three epochs. We found T_{Moon} to be at 184.4 ± 2.6 K and 173.8 ± 2.5 K using the first and the second methods, respectively, and the best-fit values of the Galactic spectral index (α) to be within the 5% uncertainty level when compared with the global sky models. Compared with our previous work, these results improved constraints on the Galactic spectral index and the Moon's intrinsic temperature. We also simulated the Earthshine at MWA between November and December 2023 to find suitable observing times less affected by the Earthshine. Such observing windows act as Earthshine avoidance and can be used to perform future global CD-EoR experiments using the Moon with the MWA.

Keywords: Early Universe, Cosmic Dawn and Reionization, first stars, observations, MWA**1. Introduction**

The Cosmic Dawn (CD) marked the end of the Dark Ages with the emergence of the first luminous objects in the early Universe. These objects were the first generation of stars, black holes and other compact objects. The X-ray and UV radiation produced by these objects started heating and ionising their surrounding matter. This ionising process gradually changed the state of the IGM from neutral to fully ionised during the Epoch of Reionisation (EoR) until the redshift $z \sim 5.3$ (see Furlanetto, Sokasian, and Hernquist 2004; Bharadwaj and Ali 2005; Pritchard and Loeb 2012; Mesinger 2016, for review). The observational evidence from high redshift quasar spectra (Fan et al. 2003; Barnett et al. 2017), Ly- α emitters (McQuinn et al. 2006) and Cosmic Microwave Background (CMB) scattering from the ionised IGM at low redshifts implies that the cosmic reionisation lasted between redshifts $z \approx 18 - 5.3$ (Komatsu et al. 2011; Aghanim et al. 2020). However, these studies have only placed weak constraints on the astrophysical properties of the first stars, black holes and galaxies and the evolution of the early Universe due to the difficulty of direct observations. The neutral medium of atomic Hydrogen (HI) is largely opaque to UV radiation, whereas the X-ray tends to heat the IGM; therefore, it becomes challenging to observe the CD-EoR directly at these frequencies due to absorption by the IGM. An indirect approach of using the 21-cm emission line from the leftover HI from this era is the most likely candidate

to probe the CD-EoR. (Mesinger 2016)

The 21-cm signal arises from the spontaneous transition of Hydrogen from the ground state triplet to the singlet state, causing the emission of a radio photon of ≈ 1420 MHz, which can be detectable by ground-based radio antennae. Therefore, several radio instruments, e.g. Murchison Widefield Array (MWA) (Tingay et al. 2013), Precision Array for Probing the Epoch of Reionization (PAPER) (Pober et al. 2011), Hydrogen Epoch of Reionization Array (HERA) (DeBoer et al. 2017), LOw-Frequency ARray (LOFAR) (van Haarlem and others 2013), New Extension in Nancay upgrading LOFAR (NenuFAR) (Mertens, Semelin, and Koopmans 2021), Giant Meter wave Radio Telescope (GMRT) (Paciga et al. 2013), Long Wavelength Array (LWA) (Eastwood et al. 2019) etc., aim to detect the 21-cm signal from the CD-EoR. These instruments target either the statistical features of the 21-cm signal (e.g. power spectrum) using radio interferometers, e.g. MWA (Trott et al. 2020), GMRT (Paciga et al. 2011), LOFAR (Mertens et al. 2020), HERA (Abdurashidova et al. 2021), PAPER (Parsons et al. 2014) or the volume averaged 21-cm signal (global 21-cm signal) using a single antenna, e.g. Experiment to Detect the Global EoR Signature (EDGES) (Bowman, Rogers, and Hewitt 2008; Bowman and Rogers 2010; Bowman et al. 2018), Broad-band Instrument for Global HydrOgen Reionization Signal (BIGHORNS) (Sokolowski et al. 2015), Shaped Antenna measurement of the background Radio Spec-

trum (SARAS) (Patra et al. 2012), SARAS2 (Singh et al. 2018), SARAS3 (Singh et al. 2022), Large Aperture Experiment to Detect the Dark Age (LEDA) (Bernardi et al. 2016), Dark Ages Radio Explorer (DARE) (Sigel et al. 2013) now known as Dark Ages Polarimeter Pathfinder (DAPPER) (Burns, Bale, and Bradley 2019), Sonda Cosmológica de las Islas para la Detección de Hidrógeno Neutro (SCI-HI) (Voytek et al. 2014), Probing Radio Intensity at High-Z from Marion (PRIZM) (Philip et al. 2019). However, the radiation received by these instruments is dominated by the foreground emission from the Galactic and extra-galactic radio sources. Alongside these foregrounds, instrument-based systematics, thermal noise, and radio frequency interference (RFI) present enormous challenges in 21-cm signal detection.

The global EoR experiments measure the sky-averaged strength of the 21-cm signal by estimating the total power of 21-cm brightness as a function of frequency, which represents the redshift evolution of the early Universe. The first claimed detection of the global 21-cm signal came from EDGES (Bowman et al. 2018), which found an absorption trough profile around 78 MHz, which aligned with the theoretical predictions of early cooling and reheating (Furlanetto, Oh, and Briggs 2006; Pritchard and Loeb 2012). However, recent cross-validations from the SARAS3 experiment found that EDGES detection was mainly due to systematic errors (Singh et al. 2022). This signifies that, despite the high signal-to-noise ratio (SNR) of these experiments, the non-thermal components of the receiver noise can mimic the cosmic signal of interest, leading to false detection scenarios. Therefore, minimisation of the instrumental systematics is the major goal of these experiments (Monsalve et al. 2017; Singh et al. 2017; Sokolowski et al. 2015).

An alternative approach, known as the lunar occultation method, has the potential to detect the global 21-cm signal. Instead of a single antenna or dipole, this approach utilises radio interferometers to detect the sky-averaged 21-cm signal. Interferometers, in general, are not sensitive to the global sky as the response rapidly falls off for baselines $> 1\lambda$. However, the presence of the Moon introduces a mask in the sky, which helps sustain the coherence in the global sky response at longer baselines ($> 50\lambda$) (see fig. 1 from Vedantham et al. (2015) for reference). The idea of lunar occultation was first proposed by Shaver et al. (1999) and has been implemented by McKinley et al. (2012) and McKinley et al. (2018) on MWA, and Vedantham et al. (2015) on LOFAR. In lunar occultation, the Moon is treated as a thermal block in the sky, and the interferometer measures the difference between the Moon's temperature and the global sky temperature. The benefits of using interferometers are that they contain independent antenna elements, and the voltage correlations at their receivers are devoid of frequency-dependent receiver-noise bias. Also, unlike single antenna or dipole-based experiments, which measure and mitigate the entire foreground sky to detect the global 21-cm signal, the lunar occultation method only measures the patch of sky occulted by the Moon and hence is only required to mitigate the foregrounds occulted by the Moon. This significantly reduces the Galactic emission and spectral index anomalies,

which otherwise are very difficult to deal with. Therefore, lunar occultation can be used to cross-validate the findings from the EDGES and SARAS-3 experiments, and since more sensitive instruments, such as MWA phase II & III, are currently functional, and the upcoming SKA operations are also on the horizon, it is worth further investigating the lunar occultation approach for CD-EoR science.

In this work, we extended the approach of McKinley et al. (2018) by incorporating multiple nights of higher (time and frequency) resolution MWA-phase I data. We also used a new simulation-based approach to model the reflected RFI (Earthshine) in the FM band (88-110 MHz) to mitigate the reflected FM response from the Moon. Using these two approaches, we obtained improved constraints on the Moon's intrinsic temperature, the Galactic foreground temperature and spectral index. This paper is organised as follows: In §2, we briefly summarise the lunar occultation technique. In §3 and §4, we provide information about the MWA phase-I observations and data processing techniques used in this work. In §5, we describe our approach to modelling the reflected RFI from the Moon (Earthshine). In §6, we provide the main results and discuss them in §7 along with the limitations and potential aspects of our project, and finally, we provide the conclusion in §8.

2. Background

Lunar occultation provides a unique way to detect the EoR 21-cm global signal using radio interferometers. In the radio frequencies corresponding to the CD-EoR, the Moon is treated as a thermal source at a constant blackbody temperature. The interferometer measures the difference between the Moon's temperature and the background sky temperature of the patch of sky occulted by the Moon. This can be expressed as,

$$\Delta T(\nu) = T_{\text{Lunar}}(\nu) - T_{\text{sky}}(\nu) = \frac{c^2 S_m(\nu)}{2k_B \nu^2 \Omega} \text{ K} \quad (1)$$

where S_m is the observed flux density of the Moon, Ω is the Moon's solid angle, k_B is Boltzmann's constant, c is the speed of light, and ν is the frequency. The Moon reflects a part of the Galactic foreground and terrestrial radio emission back to the observer on the Earth (Evans 1969). Therefore, the Moon's temperature includes two additional factors; the reflected Galactic foreground and reflected RFI. Thus, we can express eq.1 as,

$$\begin{aligned} \Delta T(\nu) &= T_{\text{Lunar}}(\nu) - T_{\text{sky}}(\nu) \\ &= [T_{\text{Moon}} + T_{\text{refl-Earth}}(\nu) + T_{\text{refl-Gal}}(\nu)] \\ &\quad - [T_{\text{Gal}}(\nu) + T_{\text{CMB}} + T_{\text{EoR}}(\nu)], \quad (2) \end{aligned}$$

where T_{Moon} is the intrinsic temperature of the Moon, $T_{\text{refl-Earth}}(\nu)$, is the reflected RFI (Earthshine) temperature, $T_{\text{refl-Gal}}(\nu)$ is the reflected Galactic temperature. The sky temperature $T_{\text{sky}}(\nu)$ includes the contribution from the Galactic temperature $T_{\text{Gal}}(\nu)$ (temperature of the occulted patch of the sky), Cosmic Microwave Background temperature T_{CMB} and

EoR 21-cm global sky temperature T_{EoR} . We used $T_{\text{CMB}} \approx 2.725$ K (Mather et al. 1994) in our analysis.

In most cosmic reionisation scenarios predicted by the reionisation models, the global 21-cm signal goes through major phase transitions between 88–110 MHz; however, in this band, the Moon temperature is hugely contaminated by the Earthshine. Therefore, the first step in the detection of the global 21-cm signal would be to mitigate FM reflections from the Moon. In a similar fashion, the Galactic foregrounds would be required to be mitigated in the subsequent steps, and once all components from the Moon are successfully evaluated, the T_{EoR} can be isolated from the Moon.

3. Observations

In this work, we used six nights of MWA-phase I data from 2015. Our observational strategy was to observe the same patch of sky on two different nights at the same (Local Sidereal Time) LST, where the Moon was present on one night (ON-Moon) and absent on the other (OFF-Moon). These observations were typically separated by two to three days and observed at identical LST (LST-locked). The benefit of using these LST-locked observations is to eliminate artefacts and sidelobes from the sources in the observed field by taking the difference between the ON and OFF-Moon images. The six nights of observations were carried out on 30th August, 26th September and 21st December for the ON-Moon and on 2nd September, 29th September and 24th December 2015 for the OFF-Moon, respectively (see observation table 1). Throughout this paper, we used the nomenclature of Epochs 1,2 and 3 to represent the ON-OFF Moon (paired) datasets from August, September and December, respectively.

The effect of ionospheric activity can cause a significant difference in the flux and positional offsets of sources over the period of two nights. However, studies of ionospheric activity have shown that the majority of these effects are minimal at the MRO (Jordan et al. 2017; Trott et al. 2018). We did not see a significantly bad ionospheric shift, flux anomalies or positional offsets in our data. Therefore, we ignored the effects of the ionosphere on the data. The MWA uses discrete analog beamformer settings to track the Moon and takes the observation in 30.72 MHz contiguous bands, resetting the beamformer settings close to the Moon’s location after every observation. This is known as the drift and shift tracking method (Trott 2014). A full-band 72–230 MHz observation includes 5 successive observations of such 30.72 MHz contiguous bands. In this work, we used a total of 340 observations which comprise a total of 68 full-band observations for both ON and OFF Moon from all six nights. Since each ON-Moon observation has an LST-locked OFF-Moon pair to perform the differencing, this results in a total of 34 full-band ON-OFF Moon observations. The individual observations were carried out for ≈ 230 seconds each. We processed these observations using COTTER^a (Offringa et al. 2015) for a frequency and time resolution of 40 kHz and 4 seconds, respectively. The observational details

are given in table 1. At each observation, the central fine channel and two adjacent fine channels at the edge of each 1.28 MHz coarse channel were flagged. We also flagged the combined bad dipoles/tiles from each pair of the ON-OFF Moon observations (i.e. we isolated the common working dipoles from both ON and OFF Moon observations and flagged the rest), which otherwise would have created a difference in the UV coverage on the ON and OFF-Moon observations, which could cast some additional artefacts in the final difference (ON-OFF) images. Additionally, the operating frequencies of the ORBCOMM satellites from 121–136 MHz were avoided in our analysis.

4. Data processing and modelling

The processed observations were arranged according to the ON-OFF Moon pairs and phase-shifted to the precise location of the Moon to produce difference images. We used `astropy` to locate the sky position of the Moon and shifted the phase-centre of the measurements to the location of the Moon. In order to calibrate the sky visibilities, we produced the sky model using the Positional Update and Matching Algorithm (PUMA) catalogue (Line et al. 2017) with the 800 brightest sources in the field around the Moon. The sky model was passed to `MWA-Hyperdrive`^b to perform Direction Independent (DI) calibration. The calibrated measurement sets were then used to produce primary-beam-corrected images. We used `WSCLEAN`^c (Offringa, McKinley, Hurley-Walker, et al. 2014) to produce the Stokes-I beam-corrected images from the calibrated measurement sets. Each measurement set produced 768 images corresponding to ≈ 30.72 MHz of bandwidth, with each image produced at 40 kHz frequency resolution. The images were produced with 2048×2048 pixels, with each pixel covering approximately 0.0085° , and the image spanning $\approx 17^\circ$ of the sky on each side.

The MWA’s observational strategy uses integer delays across the MWA’s 4×4 -dipole tiles (in multiple units of μ sec.) to set the beamformers. As a result, there are a limited number of “sweet-spot” pointing locations in the sky. Thus, in the majority of cases, the pointing centre of the beam was not at the precise sky position of the Moon during the observation. Since the primary beam size reduces with increasing frequency, most of the high-band observations were affected by the Moon being located beyond half power point of the beam (resulting in a low SNR). Therefore, we limited our analysis to the beam’s full-width half maximum (FWHM), discarding observations where the Moon was located beyond the FWHM. As a result, we had a full-band frequency range of our processed images from $\approx 72 - 180$ MHz.

Finally, we took the difference between the ON and the OFF Moon images and proceeded to the flux-density estimation and Earthshine mitigation processes.

The detailed radar studies of the Moon by Evans and Hagfors 1966; Evans 1969; Hogan and Rees 1979. (Evans 1969) showed that the scattering of the reflected radio power can be assumed

a. <https://github.com/MWATelescope/cotter>

b. https://github.com/MWATelescope/mwa_hyperdrive

c. <https://gitlab.com/aroffringa/wsclean>

Table 1. ON-Moon and OFF-Moon observation details.

ON – Moon							
Date	N_{obs}	$N_{\text{obs}}^{\text{full-band}}$	Bandwidth (MHz)	Freq. res. (kHz)	Time res. (sec)	Total Int. time (sec)	Obs. duration (hrs)
30 th Aug.2015	60	12	30.76	40	4	236	3.93
26 th Sept.2015	55	11	30.76	40	4	236	3.60
21 th Dec.2015	55	11	30.76	40	4	236	3.60
OFF – Moon							
2 nd Sept.2015	60	12	30.76	40	4	236	3.93
29 th Sept.2015	55	11	30.76	40	4	236	3.60
24 th Dec.2015	55	11	30.76	40	4	236	3.60
	$N_{\text{total}} = 340$	$N_{\text{total}}^{\text{full-band}} = 68$					$\text{Time}_{\text{total}}^{\text{ON-Moon}} = 11.13$

to be coming from two distinct features of the Moon’s surface. The specular reflections from the smooth Moon and the diffuse reflections from the rough Moon. These studies showed that the radar cross-section area and the reflected power of the specular component decrease with increasing frequency while the increase with increasing frequency for the diffuse component. We followed the same two-component model (previously used by McKinley et al. 2018) to estimate the reflected RFI from the Moon. The first component was a quasi-specular Earthshine component which was a point-like source in the middle of the Moon’s disk and corresponded to the reflection from the smooth surface^d, and the second component was the diffuse reflection from the rough disk of the Moon. (Note that the quasi-specular Earthshine can have a typical angular size of ≈ 16 arcsec at the centre of the Moon’s disk (Vedantham et al. (2015)), whereas the diffuse is roughly equal to the Moon’s angular size). The two-component Earthshine model can be described as:

$$s_{\text{disk}}, s_{\text{spec}} = (\mathbf{H}^T \mathbf{H})^{-1} \mathbf{H}^T \mathbf{D} \quad (3)$$

where the s_{disk} is the flux density (in Jy/pixels units) of the Moon’s disk, s_{spec} is the flux density of the quasi-specular Earthshine at the centre of the Moon, and $[\mathbf{D}]$ is the beam-corrected difference image. The vector operator \mathbf{H} is defined using the PSF $[\mathbf{P}]$ convolved over unity masks $[\mathbf{M}, \mathbf{B}]$,

$$\mathbf{H} = [\mathbf{M} * \mathbf{P} \quad \mathbf{B} * \mathbf{P}],$$

the mask \mathbf{M} represents the disk, \mathbf{B} represents the quasi-specular mask, \mathbf{P} is the PSF of the image and $*$ represents the convolution operation. The disk mask has the same angular size as the Moon, whereas the quasi-specular mask occupies 8×8 pixels at the centre of the Moon’s image. Fig.1 shows the cropped (252×252) central pixels of the difference image, the reconstructed quasi-specular component, the disk component and the residual at the middle of the FM-band ≈ 100 MHz (ν_0 , hereafter). Finally, the estimated values of s_{disk} and s_{spec} are summed over the corresponding masks to get the total flux density of the total disk and quasi-specular earthshine components.

$$S_{\text{disk}} = \sum s_{\text{disk}} \cdot \mathbf{M}; \quad S_{\text{spec}} = \sum s_{\text{spec}} \cdot \mathbf{B} \quad (4)$$

d. Moon’s disk is the 2D projection of Moon’s area

(Note that the flux density of the disk component S_{disk} includes the contribution of the flux density (S_m) of the Moon and the diffuse Earthshine (S_{diffuse}). In this work, we used two different approaches to separate the Earthshine from the Moon’s flux density. In the first approach, we followed a similar method as McKinley et al. (2018), whereas in the second, we mitigated the Earthshine by simulating the FM flux density. Finally, we estimated the flux density of the Moon, $S_m(\nu)$ from S_{disk} as described later in §6.1.

5. Earthshine Simulation

5.1 Simulation Motivation

At radio frequencies, the Moon reflects about 7% of the incident radiation falling on its surface (Evans 1969). As a result, the Moon reflects back a significant amount of the residual radiation which escapes the Earth. We can observe strong RFI reflections from the Moon in the FM band (88–110 MHz) and Digital TV (180–220 MHz). The exact behaviour of these RFI reflections is unknown, as it depends on the time and the location of the Moon and the observatory during the observation. Therefore, simulating the reflected radiation from the Moon in the context of MWA’s Moon observations can be useful in understanding the nature of the reflected RFI from the Moon. In addition, the simulations can help investigate the RFI reflections at different LSTs, which can be used to identify the minimal RFI imprint during the observation window and help in scheduling future observations.

5.2 Simulation Method

In this analysis, we used a catalogue of FM stations^e to estimate the reflected Earthshine from the Moon. The catalogue contains information on the location of $\approx 171,000$ FM stations across the Earth, including their operating frequencies and transmitting powers. In modelling the simulated Earthshine, we made a few assumptions based on inadequate information on the beam pattern and operating hours of the FM stations in the catalogue. We assumed that all FM stations transmit isotropically throughout the full day. Due to the isotropic beam assumption, the reflected RFI includes the contribution from all of the FM stations where the Moon was above the

e. <https://fmlist.org>

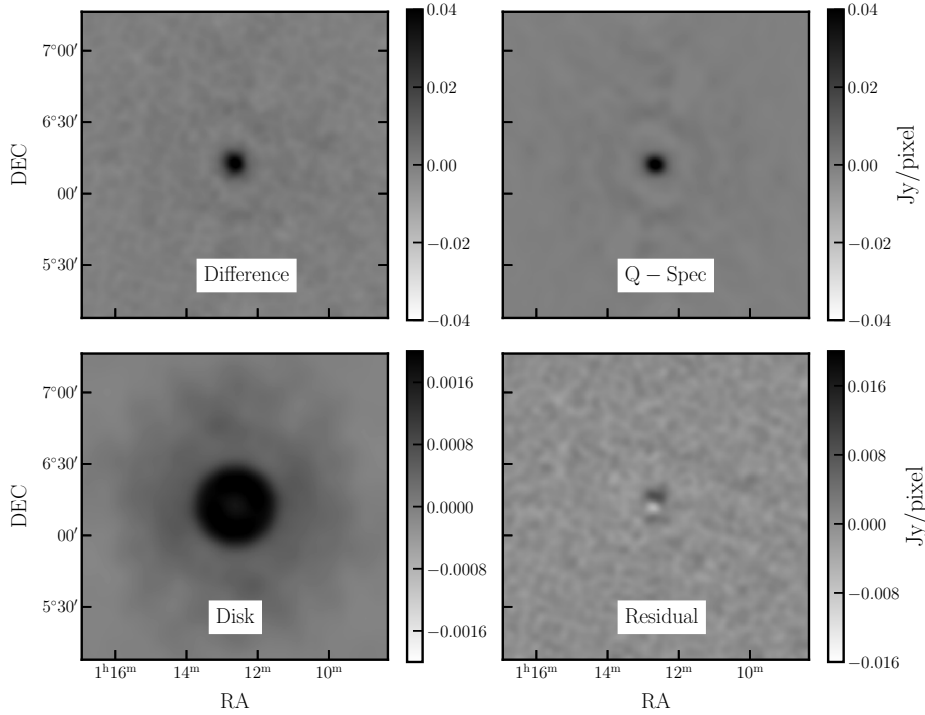


Figure 1. {Top panel} Left: Difference image of the ON-OFF observation, Right: The reconstructed model of the quasi-specular Earthshine component obtained by multiplying s_{spec} with quasi-specular mask [B]. {Bottom panel}, Left: The reconstructed disk of the Moon is obtained by operating the PSF [P] to the disk mask [M], Right: The residual image, obtained by subtracting the reconstructed disk and specular Earthshine components from the difference image. The shown images are the average of all components from the second observational Epoch (Sept. 2015) at the middle of the FM band ($\approx \nu_0 = 100$ MHz)

horizon at their location at the time of ON-Moon observation. Fig. 2 shows the location of all the stations appearing above the horizon as viewed from the Moon at the time of observation on the world map.

FM broadcasting follows different operating standards in different countries; therefore, the bandwidth of FM stations varies worldwide. We followed the conservative approach of Carson’s rule (Carson 1922) to estimate the bandwidth of FM stations and assumed that all FM stations have the same frequency deviation of 75 kHz with a modulation frequency of 15 kHz. It provided us with a bandwidth ΔB of 180 kHz (see Chapter 4 from Haykin (1989) for reference). We assumed all stations transmit a constant power across ΔB . Finally, we estimated the reflected FM flux density from all the contributing FM stations at the MWA location using the following equation:

$$S_{\text{FM}}(\nu) = \frac{P_{\text{rec}}(\nu)}{\Delta B A_{\text{eff}}}, \quad (5)$$

where $P_{\text{rec}}(\nu)$ is the received power defined as radar equation (eq. 24 Evans 1969)

$$P_{\text{rec}}(\nu) = \frac{P_{\text{emit}}(\nu) \sigma_{\text{cross}} A_{\text{eff}}}{(4\pi)^2 D_1^2 D_2^2},$$

where $P_{\text{emit}}(\nu)$ is the transmitted power, D_1 is the distance between the FM station to the Moon, D_2 is the distance from the Moon to the MWA, ΔB is the transmission bandwidth, and A_{eff} is the effective area of the MWA telescope.

$\sigma_{\text{cross}} = 0.081\pi R_{\text{Moon}}^2$ is the radar cross-section area; it includes the contribution of 7% of Moon’s albedo (Evans 1969). We sampled our simulation at every 40 kHz to match the frequency resolution of the data.

6. Results

6.1 Estimating $S_m(\nu)$

In the previous steps of modelling (§4), we separated out the specular component from the Moon. The removal of the remaining diffuse component (S_{diffuse}) will provide an estimate of the flux density of the Moon ($S_m(\nu)$),

$$S_m(\nu) = S_{\text{disk}}(\nu) - S_{\text{diffuse}}(\nu) \quad (6)$$

The reflected power of the specular and the diffuse components have a frequency dependence (see eq. 31 and 32 from Evans 1969). Applying these equations to the radar equation (eq. 24 from Evans 1969, or a similar equation described herein 5.2), one can describe a relation between specular and diffuse components as,

$$S_{\text{diffuse}}(\nu) = R_c(\nu) S_{\text{spec}}(\nu) \quad (7)$$

Due to the usefulness of the FM band in our analysis, we defined $R_c(\nu)$ for a scaling frequency ($\nu_0 = 100$ MHz) in the middle of the FM band, with the power-law index 0.58 arriving from the frequency dependence (see eq. 31 and 32

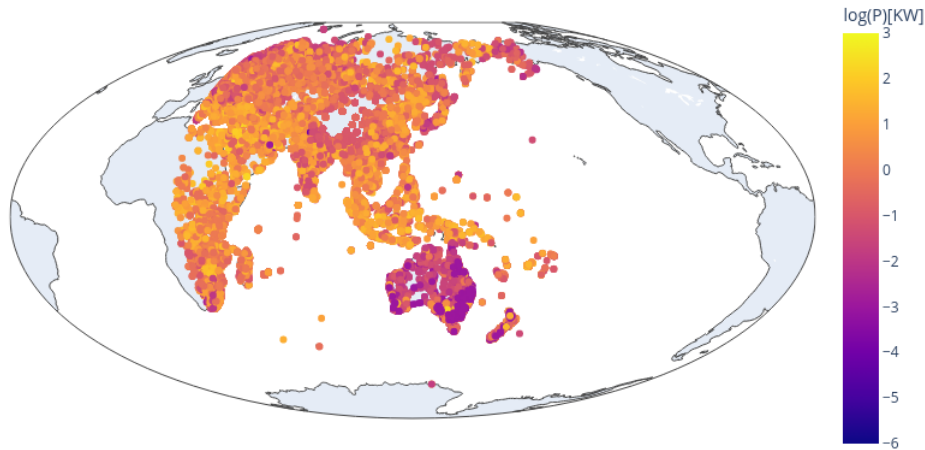


Figure 2. The locations of FM stations considered for the reflected RFI estimation during the ON-Moon observation. The figure represents a single snapshot in the middle of the second observation epoch (Sept. 2015). The colourbar represents the transmitting power of the stations in kW. The figure represents all the stations from where the Moon is above the horizon at the time of ON-Moon MWA observation.

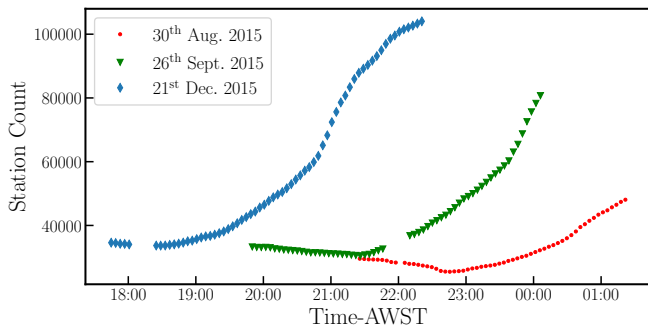


Figure 3. The variation of FM station count during the ON-Moon observations made on all three Epochs (30th August, 26th September and 21st December 2015). It can be seen that the station counts change significantly on all three epochs during the observation. The data points are generated every ≈ 230 seconds to match the observation time.

from Evans 1969).

$$R_e(\nu) = \frac{S_{\text{diffuse}}(\nu_0)}{S_{\text{spec}}(\nu_0)} \left(\frac{\nu}{\nu_0} \right)^{0.58}, \nu_0 = 100 \text{ MHz} \quad (8)$$

Once the $S_{\text{diffuse}}(\nu)$ is estimated $S_m(\nu)$ can be evaluated using eq. 6. Next describes the two methods we used to estimate $S_{\text{diffuse}}(\nu)$ as the final Earthshine mitigation step before estimating the foreground sky temperatures.

6.1.1 From DATA

In the first method, the flux-density $S_{\text{diffuse}}(\nu_0)$ is obtained by fitting a line to the $S_{\text{disk}}(\nu)$ component (see fig.4, yellow fitted line on the top panel). The fitted value at ν_0 represents $S_m(\nu_0)$, and rearranging eq.6 can provide $S_{\text{diffuse}}(\nu_0)$. Once

we obtained the $R_e(\nu)$, we plugged it into eq.7 and determined $S_{\text{diffuse}}(\nu)$ for the entire frequency band, and finally we remove the Earthshine component $S_{\text{diffuse}}(\nu)$ from the $S_{\text{disk}}(\nu)$ and estimated $S_m(\nu)$ using eq. 6.

6.1.2 From Simulation

In the Earthshine simulations, we first calculated the number of FM stations from where the Moon was above the horizon. This was used to estimate the total RFI reflection from the disk of the Moon. It can be seen (see fig. 13) that the reflected flux density received at the MWA increases with increasing station count. For an entire ON-Moon observation epoch, we simulated the Earthshine for every ON-Moon observation (see the variation of FM station counts as it changes over the entire observation duration of ≈ 3 hours in fig. 3). However, in our analysis, we used the simulated Earthshine only at those timestamps when our ON-Moon observations were in the FM band (i.e. when the 30.72 MHz contiguous band included the FM frequencies). The simulated Earthshine flux density can be used to replace the flux density from the data in the FM band (here, we refer to S_{diffuse} between 88 – 110 MHz as the data which were evaluated using eq. 7).

To statistically quantify the simulations and the data we performed a simple T-test on the data and the simulation. Our null hypothesis was based on the argument that the two discrete samples are drawn from the same distribution. We used the T-test with a confidence of 95%, which means we rejected the null hypothesis if the p -values were less than 0.05 and accepted otherwise. Our sample set comprised the LST variation (across a given observing epoch) of the flux density of the data and simulation with the frequency resolution of 40 kHz and matching LST cadence to the observing epochs

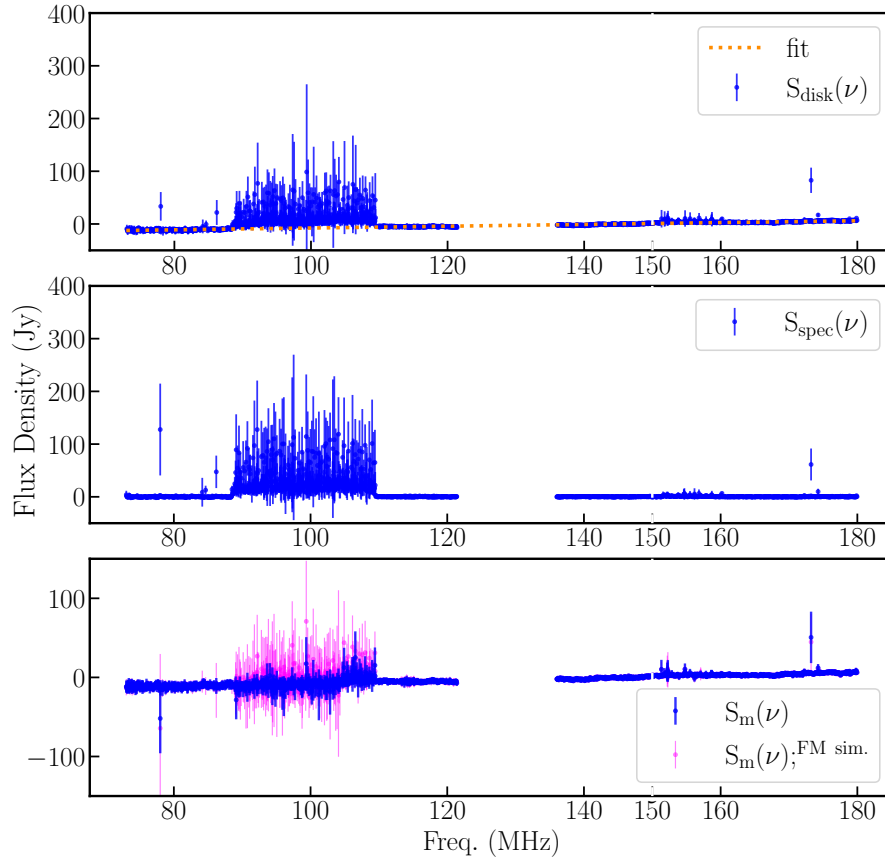


Figure 4. The observed flux density of the disk component in the top panel and the quasi-specular Earthshine component in the middle panel. The bottom panel shows the flux density of the Moon after performing the Earthshine mitigation using two methods. The *blue* errorbars correspond to the Earthshine mitigation of the first kind, where we used the fitted value of $S_{\text{diffuse}}(\nu)$ at ν_0 to determine $S_m(\nu)$. The line fitted to the disk component is shown with *yellow* dashes in the top panel. The second method is shown by the *pink* errorbars, where the simulated value of $S_{\text{diffuse}}(\nu)$ at ν_0 is used to estimate $S_m(\nu)$. The data points are at 40 kHz fine channels and averaged over 12 full-band MWA observations from the first epoch. The corresponding errors are obtained using the inverse variance weighted scheme. The *black* vertical dashed line is at 150 MHz, which corresponds to the frequency where the Moon first appears in emission.

(note that while estimating the simulated flux density we did not account for the integration time but rather estimated the instantaneous flux density at the middle of each observation). The S_{diffuse} from the data is obtained by performing a similar fitting (mentioned as the first approach) to S_{disk} for all 34 full-band individually which also provides the LST variation of S_{diffuse} . Once the flux density S_{diffuse} , S_{FM} for every individual epoch is evaluated we performed the T-test between them at every 40 kHz fine channel independently. The estimated p -values on the dataset from the first epoch are shown in fig. 14. As we are limited by our FM catalogue and simulations, our null hypothesis was rejected in nearly half of the fine frequency channels. We note that the simulations were generated at the frequency resolution of the data (i.e. 40 kHz) with the assumption that the FM stations transmit constant power throughout the 180 kHz bandwidth, so a constant flux density was estimated by the simulations, which is not true in case of the data (see fig. 5 showing the flux-density of the data (S_{diffuse}) and simulation (S_{FM})). Therefore, instead of directly subtracting the reflected diffuse FM RFI component from the data, we restricted our analysis to the single frequency channel, in particular, the central FM band ($\approx \nu_0$) and evaluated the

$R_e(\nu)$ (from eq.8) to perform the Earthshine mitigation. The estimated p -values at the middle of the FM band ($\approx \nu_0$) are presented in Table 2.

Table 2. p -values from the T-test at the middle of the FM band $\approx \nu_0$.

Epochs	p -value at ($\approx \nu_0$)
Aug.	0.75
Sept.	0.69
Nov.	0.78

Since the p -values at ν_0 satisfy our null hypothesis, in the second method of Earthshine mitigation, we used the simulated value of $S_{\text{FM}}(\nu_0)$ as the $S_{\text{diffuse}}(\nu_0)$ and estimated $R_e(\nu)$ and used it in eq.7 and eq.6 to determine $S_m(\nu)$. The flux density of the Moon obtained via both methods is shown in fig.4.

In both methods of Earthshine mitigation, we obtained the values of $S_m(\nu)$ for every 34 full-band observations separately, and to obtain the uncertainties in $\Delta S_m(\nu)$. We used the RMS noise of the disk and quasi-specular components, the analysis of which is presented in the appendix. Finally, we used the inverse-variance weights to obtain the mean and variance in

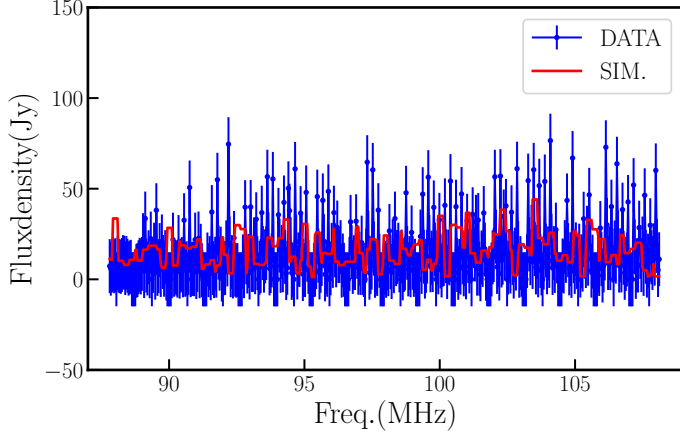


Figure 5. The mean flux density of the data and simulation in the FM band at the first observing epoch.

$S_m(\nu)$. We averaged $S_m(\nu)$ according to their corresponding epochs. As a result, we had 3 realisations of $S_m(\nu)$ for the corresponding 3 ON-Moon observing nights which were used in eq.1 to find the temperature difference $\Delta T(\nu)$.

6.2 Estimating $T_{\text{refl-Gal}}(\nu)$

We used a similar vector ray-tracing algorithm to McKinley et al. (2018) to estimate the reflected Galactic emission from the Moon. The algorithm assumes that the observatory is located on the Moon and generates the sky map as observed from the Moon. The part of the sky map that reflects back to MWA’s location is determined by estimating the angle of incidence and reflection of the sky map at the Moon’s surface based on the radar cross-section criteria. We used Python-based PYGDSM to produce the Low-Frequency Survey Model (LFSM) (Dowell et al. 2017), Haslam (Remazeilles et al. 2015), Global Sky Model 2008 (de Oliveira-Costa et al. 2008), Global Sky Model 2016 (Zheng et al. 2017) models for all three ON-Moon observation epochs. The sky models were then injected into our algorithm to produce the reflected sky map from the Moon. The reflected sky does not change significantly during our observational epochs (spanning approx 2 – 3 hours), as the Moon sweeps only about ($\approx 1^\circ - 1.5^\circ$) on the sky during each epoch. Therefore, we used the middle point of time at each MWA’s full band observations to estimate the reflected Galactic temperature. We produced the sky maps at every 5 MHz frequency channel from 70 – 180 MHz. Fig. 6 shows the reflected Galactic temperature $T_{\text{refl-Gal}}$ at 150 MHz in the middle of the first ON-Moon observation epoch. $T_{\text{refl-Gal}}(\nu)$ follows a power law, and it can be shown that the reflected Galactic temperature fits well with the power-law equation:

$$T_{\text{refl-Gal}}(\nu) = T_{\text{refl-Gal150}} \left(\frac{\nu}{150\text{MHz}} \right)^\beta \quad (9)$$

The spectral index β is obtained by fitting the mean and 5% model error (Zheng et al. 2017) of the reflected Galactic temperature to the power-law equation. Fig.7 shows the re-

flected Galactic temperature for all of the three epochs. The fitted values of $T_{\text{refl-Gal150}}$ and β , are provided in Table 3.

Table 3. Showing the fitted values of the $T_{\text{refl-Gal150}}$ and reflected Galactic spectral index β .

Epochs	$T_{\text{refl-Gal150; GSM2016}}$	β_{GSM2016}
Aug.	$23.83 \pm 1.19\text{K}$	-2.541 ± 0.003
Sept.	$19.64 \pm 0.98\text{K}$	-2.562 ± 0.003
Nov.	$27.41 \pm 1.37\text{K}$	-2.511 ± 0.003

6.3 Estimating T_{Moon} and $T_{\text{Gal}}(\nu)$

So far, we have evaluated the quantities ΔT , $T_{\text{refl-Earth}}$ and $T_{\text{refl-Gal}}$ of eq.2. Note that the $T_{\text{refl-Earth}}$ has already been removed from the data during the Earthshine mitigation process (described in the previous section §6.1). Therefore, we are left with the $T_{\text{Gal}}(\nu)$, $T_{\text{Moon}}(\nu)$, $T_{\text{EoR}}(\nu)$ and T_{CMB} variables. Our present analysis focuses on combining the observations from different epochs and checking whether we can produce better constraints on the Moon’s intrinsic temperature from our previous work. Detecting the EoR would require proper foreground modelling, more observations to increase the SNR of the occulted sky patch and improved Earthshine models, which we aim to address in future works. Therefore, we ignore the contribution of EoR in the sky temperature. The remaining variables $T_{\text{Gal}}(\nu)$ and T_{Moon} , are the temperature of the occulted patch of sky and the intrinsic temperature of the Moon, respectively. The variables in eq.1 can be rearranged to:

$$T_{\text{Gal}}(\nu) - T_{\text{Moon}} = T_{\text{refl-Gal}}(\nu) - \Delta T(\nu) - T_{\text{CMB}} \quad (10)$$

Here we have information on the RHS variables of the equation, and as we considered the Moon to be at a constant temperature, it will act as a temperature offset to the LHS. We fit the temperature difference between the Galactic emission and Moon with a similar power law from eq. 9, but with a constant temperature offset (T_{offset}).

$$T_{\text{Gal}}(\nu) - T_{\text{Moon}} = T_{\text{Gal150}} \left(\frac{\nu}{150\text{MHz}} \right)^\alpha - T_{\text{offset}} \quad (11)$$

6.3.1 Fitting for T_{Moon} (Individual Epochs)

In order to obtain T_{Moon} , first, we estimated the model values of the $T_{\text{Gal}}(\nu)$, and we followed the same procedure as for $T_{\text{refl-Gal}}(\nu)$. We generated the GSM, GSM2016, LFSM and Haslam maps at the frequency resolution of 5 MHz for all ON-Moon observations and estimated the $T_{\text{Gal}}(\nu)$ of the patch of sky occulted by the Moon.

We fit the model Galactic temperature with a similar power-law equation to $T_{\text{refl-Gal}}$ (see §Appendix 1.2 and eq.15, and obtained the values of $T_{\text{Gal150; sky-model}}$, and $\alpha_{\text{Gal150; sky-model}}$. In fig.8, we show the data from the first epoch. The $T_{\text{Gal}}(\nu)$ is estimated using both methods of Earthshine mitigation, and the fitted values of $T_{\text{Gal}}(\nu)$ at 150 MHz and the Galactic spectral

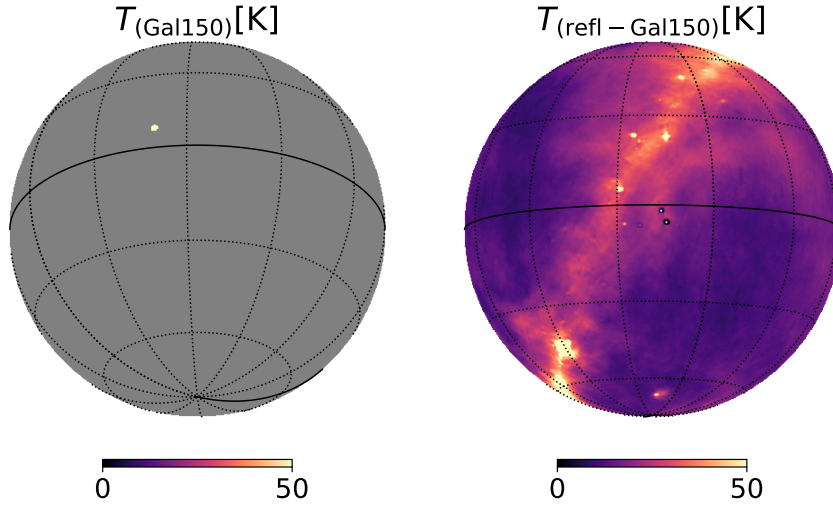


Figure 6. Galactic temperature from the GSM2016 model at the middle of the second epoch. The left panel shows the occulted sky temperature T_{Gal150} as observed from the MWA. The single dot represents the location of the Moon during the ON-Moon observation. The right panel shows the sky temperature reflected by the Moon $T_{\text{refl-Gal}}$. To make the pixels visible on the left figure, we doubled the pixel counts of the Moon and saturated the colourbar by using the same colour scale as the right figure.

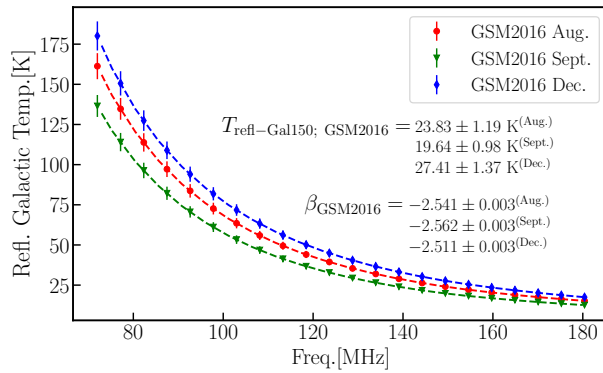


Figure 7. Mean reflected Galactic temperature estimated using GSM2016 (Zheng et al. 2017) at all three epochs. The reflected Galactic temperature (shown by point, triangle, and diamond markers) is fitted with the power law eq.9. It can be seen that the reflected Galactic temperature at 150 MHz ($T_{\text{refl-Gal150}}$) does not change significantly between the epochs. The error bars corresponding to $T_{\text{refl-Gal150}}$ represent the 5% model estimation error of GSM2016 (Zheng et al. 2017), and the uncertainty in the β represents the fitting error.

index (α) are presented for the data and GSM2016 model. A comprehensive table showing the fitted values of $T_{\text{Gal}}(\nu = 150 \text{ MHz})$ and T_{Moon} estimates from all sky models is given in the appendix (see 7). Please note that, in order to get the fitting for T_{Moon} and T_{Gal150} for a given sky model, we first estimated the reflected sky temperature from the same sky model and repropagated it through eq. 10 and 11.

6.3.2 Joint Fitting for T_{Moon}

We combined the measured values of $\Delta T(\nu)$ from all three epochs and performed a joint fit to eq.11. We placed restrictions on the T_{Moon} and considered the Moon to have a constant temperature. In the joint fit of the data to eq.11, there is a total of six independent and one dependent parameter. The best-fit values of T_{Gal150} , spectral index α and T_{Moon} , along with the estimations of the sky models, are presented in Table 4. The results presented in Table 4 are for both the Earthshine mitigation approaches. The table also shows the expected Galactic foreground temperature and the spectral index (obtained from the GSM2016 model (Zheng et al. 2017)) of the patch of sky occulted by the Moon during these observations. Please note that the larger error bars in fig.(8, 9, 10) at the lower frequencies could arise due to several factors, the first being the observations itself. Since the Moon moves $\approx 6.5^\circ$ with respect to the background sky during a single night, the mean occulted galactic temperature obtained over multiple individual spectra shows a larger deviation. Second, the thermal noise and the noise from the sidelobe confusion are more at the lower frequencies. In general, the sky noise is dominated by the lower frequencies.

7. Discussion

As the $T_{\text{Gal}}(\nu)$, T_{Moon} and the spectral index α are deduced from the same fitting function, these parameters are highly correlated with each other. The correlation amongst the parameters from the joint analysis for the first method of Earthshine mitigation is shown in Table 6. We aim to deal with these degeneracies in future work when we include the observational datasets from the Engineering Development Array (EDA) (Wayth et al. 2017) and measure the Moon temperature independently, which can provide better constraints on the Galactic foregrounds. Our finding of the Moon's temperature,

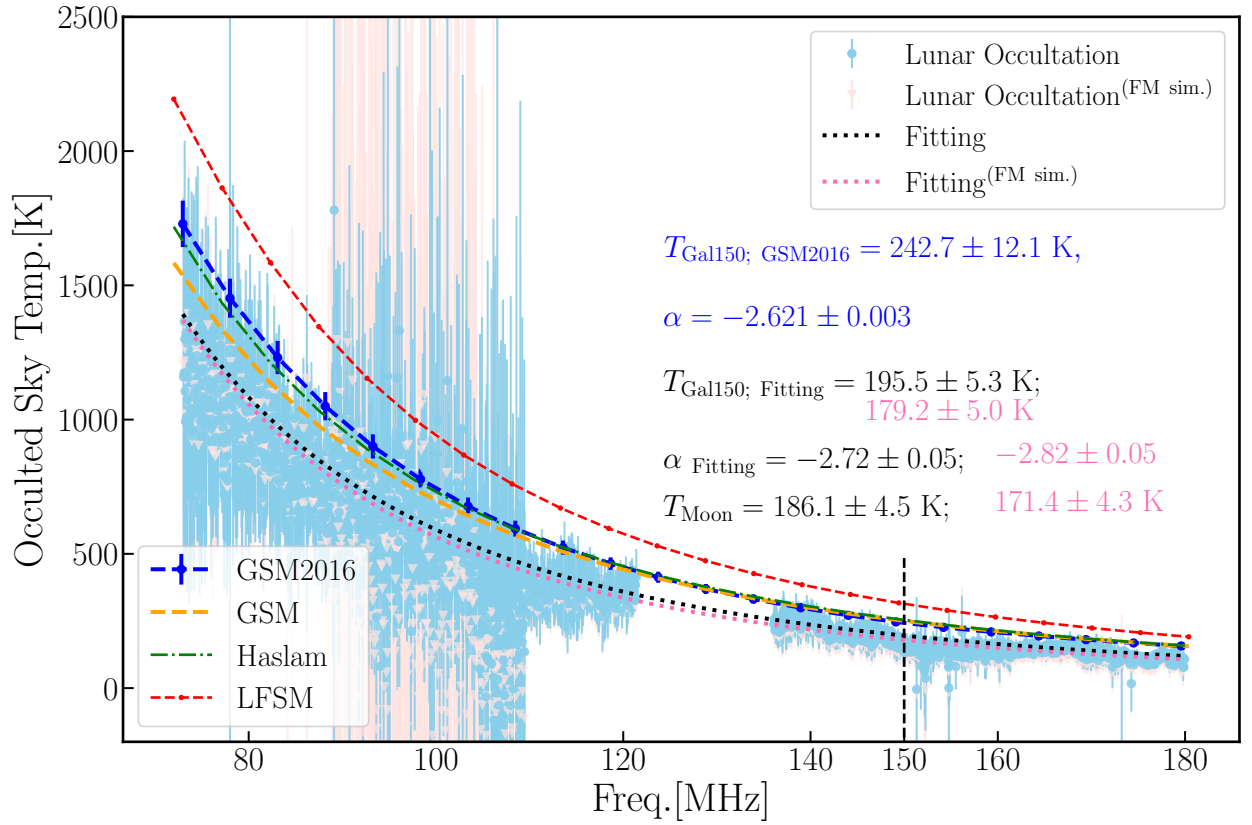


Figure 8. Occulted sky temperature from the dataset from the first epoch. The data points shown by *light blue* and *light pink* represent the occulted sky temperature obtained using the two Earthshine mitigation methods. The data points fitted with $T_{\text{Gal}}(\nu)$, are shown by the dashed lines (*black* and *pink*) for the respective methods. The quoted values of the $T_{\text{Gal150; Fitting}}$, α_{Fitting} and T_{Moon} are obtained by taking the inverse-variance weighted mean and variance. For comparison, different GSM sky models are plotted over the data points. The model uncertainty in the Galactic temperature and spectral index of GSM2016 are shown in the *blue* text in the figure.

along with McKinley et al. (2018) and results from Table 2 of Krotikov and Troitskii (1964), are shown in fig.11. In our joint analysis, we obtained the Moon temperature from the first method to be $184.4 \pm 2.6\text{K}$ and $173.8 \pm 2.5\text{K}$ from the second method, respectively. These estimates are inconsistent with each other. The deviation in T_{moon} between the two methods is $\approx 10\text{K}$, which could be due to imperfect simulations; however, these results put tighter constraints on the Moon temperature and agree with the results of McKinley et al. (2018), which predicted $T_{\text{moon}} = 180 \pm 12\text{K}$. On the other hand, similar to McKinley et al. (2018), our estimates of the occulted sky temperature at 150 MHz (T_{Gal150}) underestimated the model predictions. Our results agree within 2σ uncertainty levels when compared with the GSM2016 sky model (Zheng et al. 2017) (note that here we used the σ levels by considering the uncertainties as Gaussian around the mean predicted values of T_{Gal150}).

When we compared our best-case scenario for a single epoch with the GSM2016 model, our estimates of T_{Gal150}

had $\approx 19\%$ error with the model predictions. In comparison, the same was $\approx 12\%$ in McKinley et al. (2018) results. It can be argued that our frequency resolution of 40 kHz, which is higher compared to McKinley et al. (2018) (1.28 MHz), could have provided excess noise in the flux density estimation. The Galactic spectral index (α), when compared to the corresponding GSM2016 predicted values, agrees within 5% uncertainty levels in all three observation scenarios in the first method and 7% uncertainty in the second method. The spectral index measured at all three epochs is consistent with the findings of McKinley et al. (2018). When comparing the spectral index from other global sky models (see. fig.8), our results agreed, except for the LFSM, which predicted a higher steepness. We note that the spectral index changes from one part of the sky to another.

We compared our joint-fit results with the individual fits to the epochs. Since the three epochs are at different LSTs, one can argue how the joint fit will affect the T_{Gal150} estimates of individual epochs. We see that the deviation in the mean

Table 4. Table showing the best-fit parameters from the joint-fitting of the combined epochs.

Method 1					
Epochs	$T_{\{\text{Gal150; GSM2016}\}} \text{ (K)}$	α_{GSM2016}	$T_{\{\text{Gal150; fitting}\}} \text{ (K)}$	α_{fitting}	$T_{\{\text{Moon}\}} \text{ (K)}$
Aug.	242.7 ± 12.1	-2.621 ± 0.003	192.4 ± 3.1	-2.745 ± 0.031	184.4 ± 2.6
Sept.	241.0 ± 12.0	-2.585 ± 0.002	171.3 ± 2.8	-2.598 ± 0.033	
Dec.	380.4 ± 19.0	-2.497 ± 0.002	243.5 ± 2.9	-2.612 ± 0.022	
Method 2 (FM sim.)					
Aug.	242.7 ± 12.1	-2.621 ± 0.003	179.1 ± 2.9	-2.798 ± 0.033	173.8 ± 2.5
Sept.	241.0 ± 12.0	-2.585 ± 0.002	159.1 ± 2.7	-2.640 ± 0.034	
Dec.	380.4 ± 19.0	-2.497 ± 0.002	232.0 ± 2.7	-2.661 ± 0.021	

temperature estimates from the individual epoch T_{Gal150} to the jointly fitted values is only about 2–3K (about 1–2 per cent) and agrees with the estimated uncertainties. A comprehensive table 7 in the appendix section shows the individual fitting cases to all models. We also compared the joint T_{Moon} estimates from all the sky models. The variation in the joint T_{Moon} estimates is about 1–2 K between different models. Although all cases are consistent with each other, the GSM2016 model provides the best estimates of the uncertainties. Table 8 (Left) shows the T_{Moon} estimates from all sky models. Since the Earthshine significantly contaminates the FM band, a rectification of the data, discarding the FM and other RFI-affected bands, can be made to check whether it improves our estimates or not. Although the FM frequencies are expected to cover a crucial portion of the CD-EoR phase transition, we compared the estimates of full-band with the FM-removed cases as a test case scenario for the GSM2016 sky model. We found that for the individual epochs, the fitting uncertainties on the Galactic Temperature and Moon Temperature have variations of only about 1–2 K, while the mean temperature varies from 1–10 K. Also, the joint estimate of the same yields similar levels of uncertainty. The constraints from full-band and test-case can be considered up to a similar level since both are consistent within the estimated uncertainty. However, it can be seen that discarding the FM band neither improves the estimates and nor significantly underestimates the occulted sky temperature. Table 8 (Right) shows the fitted values of T_{Moon} and T_{Gal150} for the FM-removed scenario.

At present, we used three different nights of MWA-phase I data. However, it would be valuable to see whether the same method can be used to assimilate multiple nights and perform foreground mitigations. We leave this to future works, where we aim to include more observations from different observing nights and with varying Moon elevations with respect to the Galactic plane.

7.1 Limitations

In this part, we address various limitations of our present work, which can be dealt with in future works. Our present work includes MWA-phase I observations from multiple nights. However, in the future, the first requirement would be to check the nature of the observations before incorporating multiple datasets into the data processing. The location of the Moon

in the sky during the observation can significantly alter the quality and usefulness of the data. It would be preferred to have the Moon situated near the zenith during the ON-Moon observation (if the analysis is done based on the image plane). One limitation that we faced during our data processing was the drift and shift method of the MWA observation. As the Moon was not actively tracked by MWA, it resulted in the beam-former settings creating the beam slightly away from the location of the Moon. As a result, we had to correct the beam response in the images and perform an additional rectification on the data. We chose only datasets where the beam response was greater than that at FWHM, which limited the total integration time. The EoR signal is significantly weak compared to the foregrounds; therefore, one must deal with precise calibration of the foreground, which can create huge issues if done incorrectly. The presence of bright foreground or some missing sources in the main or side-lobes can completely contaminate the images. Therefore, better and more accurate sky models are required to get good calibration results. Also, there is a possibility that the Moon can obscure a bright foreground source during some ON-Moon observations, which can result in calibration anomalies; therefore, a careful selection of the observation is required prior to data processing. We see that the angular size of the specular RFI (number of pixels acquired by the specular reflection) at a given frequency does vary with LST. Since we used the same specular RFI mask in the modelling process, it underestimated the quasi-specular component. LSTs having a wider angular size of the specular reflection leaked a number of pixels which still were dominated by the specular RFI outside the model. This can be seen in the image residuals (see fig.1) having $\approx 10 - 15\%$ flux density to the respective quasi-specular models. We used a catalogue of FM transmitters to model the reflected power received at the MWA from all the FM stations at the time of the ON-Moon observation. We made two basic assumptions in order to generate the Earthshine. First, we assumed that the FM stations always remain active and transmit isotropically. Second, we counted all the stations from where the Moon was above the horizon at the time of the observation. Although these assumptions were made due to incomplete information on the beam patterns and operating hours of the FM stations, it certainly limits our analysis of the Earthshine mitigation using simulation (it can be seen in fig.5 that the observed flux

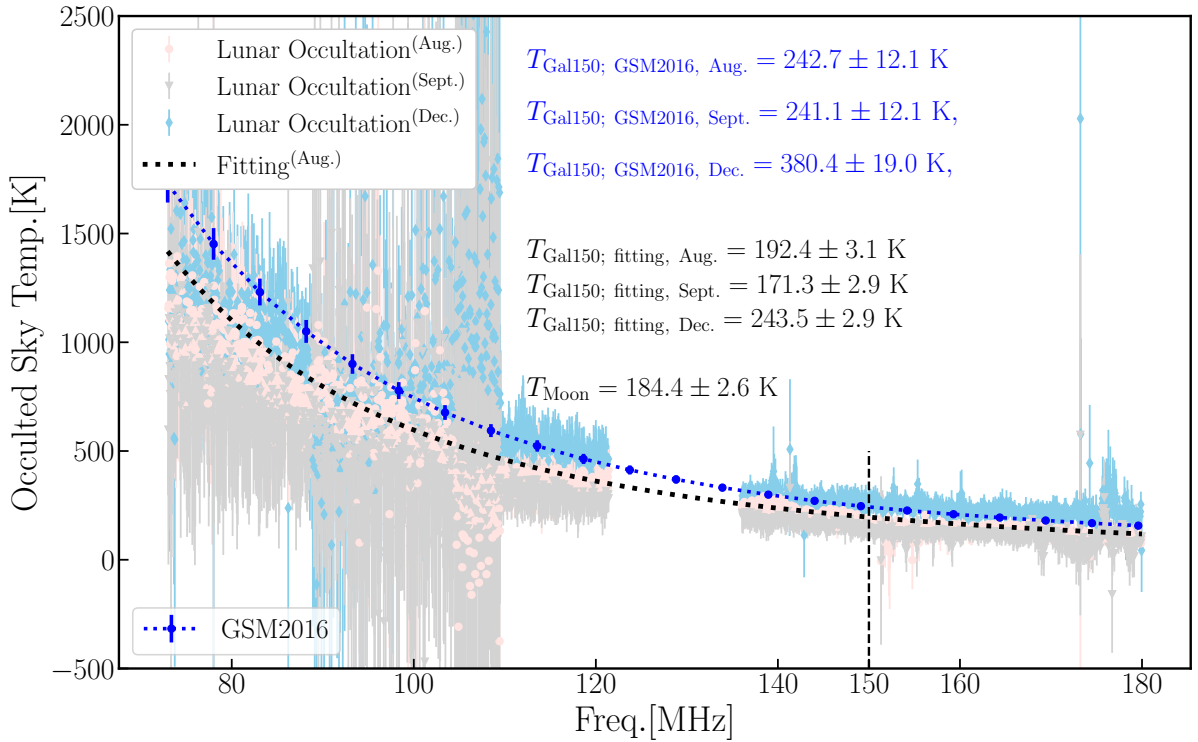


Figure 9. The data points from the three observational epochs are shown with different colour schemes (*light blue, light grey, light pink*). The *black dashed line* corresponds to the best fit to the occulted sky temperature from the first epoch (August 2015) and is plotted along with the *blue error bars* of the GSM2016. The data points and fitted values are the estimates obtained using the first method of Earthshine mitigation.

density fluctuates significantly within the assumed bandwidth of the FM stations which otherwise is constant in the simulation). In reality, the FM transmitters beam the signal along the horizontal direction and have a significant signal loss ($\approx 20\text{dB}$) within 10° tangential to the beam direction. This directivity and beam pattern of the station can significantly reduce the station counts and allow only stations having a Moon altitude of approximately 10° (near the horizon). Taking into account this effect would replace the 4π factor from the eq.5 with the beam angle θ , which can significantly alter the simulated flux density. Using that, we can also calculate the specular reflections using a vector ray tracing algorithm. We can assume a $\approx 16''$ region around the centre of the Moon to act as a smooth FM reflector and isolate the FM stations which satisfy the reflection criteria. Therefore, one can argue that the accuracy of the FM simulation would significantly alter based on the assumptions and number of factors contributing to the Earthshine.

7.2 Earthshine Avoidance

As we have seen in our simulation results (see fig. 13), increasing station count increases the overall reflected flux density from the Moon; thus, it can be said that the reflected FM from the Moon correlates with the Earth's terrestrial area (i.e. the

land area) being exposed to the Moon. In contrast, a minor reflected FM contribution would be there if the marine parts of the Earth were facing the Moon. Therefore, in Earthshine avoidance, we can use guided simulations to choose suitable observing windows when the FM station count is minimised. This would help us to reduce the strong FM RFI from the Moon, which otherwise hugely contaminates the flux received from the Moon. Fig. 12 shows a two-month simulation between November to December 2023 of the FM station count as a proxy for the reflected RFI from the Moon. The simulation targeted only the nighttime between 20 : 00 – 04 : 30 hrs. as it is relevant for our work and used the location of the Moon as seen by the MWA and FM stations. We counted only those time frames when the Moon was above the horizon at both the MWA and the FM station during the observing window (between 20 : 00 – 04 : 30 hrs) every night. There are missing data points in the middle of figure 12, which indicate that the Moon is below the horizon at the MWA site during the observing window. The station counts in the figure show repetitive behaviour over a month's time. During certain days, the station counts are significantly less than others; hence, we can utilise such time windows for scheduling future observations of the Moon.

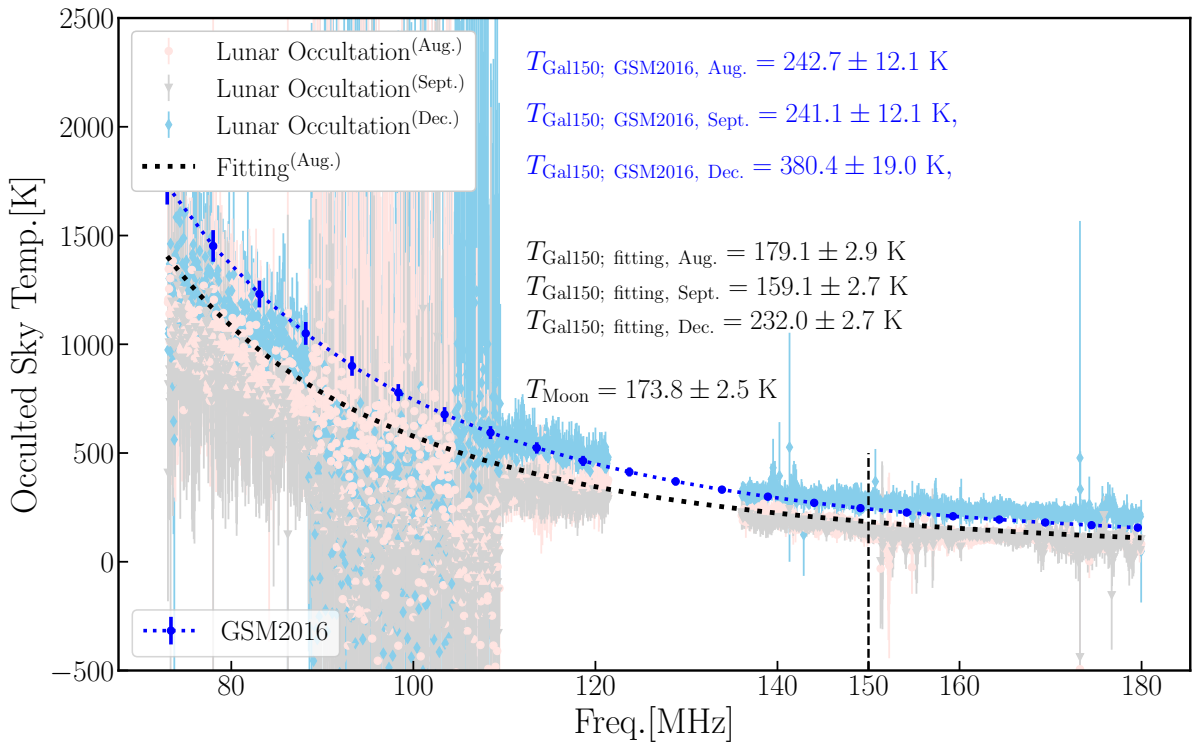


Figure 10. Occulted sky temperature measured using the second method of Earthshine mitigation (FM simulation). Data points from all three epochs are presented with coloured errorbars. The best fit to the first epoch (August 2015) dataset is plotted with the black dashed line, and the corresponding values of the GSM2016 model are plotted with the blue errorbars.

7.3 Future prospects for 21-cm signal measurements

Our current estimates motivate us to explore other techniques of Earthshine mitigation in our future work. The RFI avoidance technique might be helpful to deal with the strong reflected RFI and, therefore, can provide much-improved estimates of the observable quantities. However, we also wish to investigate whether the inclusion of the station beam patterns improves our modelling and Earthshine mitigation. In our immediate future work, we aim to analyse our latest observation of the Moon using MWA-phase II extended from 2022. MWA-phase II extended has a higher angular resolution, and it can be helpful in improving the total SNR in the FM band. Based on the results, it would be valuable to check whether we can perform foreground mitigation techniques on the phase-II data. We can utilise a similar approach as followed by the SARAS project to quantify the acceptable regimes of the global 21-cm models or alternatively explore Principle Component Analysis (PCA), Gaussian Process Regression (GPR), and Machine Learning (ML) techniques (Tauscher et al. 2021; Makinen et al. 2021; Zuo et al. 2019) to isolate the EoR component from our data. In addition to that, we can explore new techniques based on the simulations of the FM station counts during the given nights. We can choose two distinct nights where the behaviour of the station counts matches (hence the reflected

RFI), train machine learning models with the datasets from one night, and use the trained models to mitigate the Earthshine on the other. However, in such methods, the models are required to be trained up to very high accuracy. It would be worth checking the goodness of such trained models if operated on the datasets from other nights or different instruments (e.g. EDA-2).

8. Conclusion

The lunar occultation technique aims to utilise radio interferometers to estimate the sky-average global 21-cm EoR signal. However, one must accurately mitigate the Galactic foreground and reflected Earthshine in order to reach the final goal of detecting the global 21-cm signal. In this work, we used two approaches to model the FM Earthshine from the Moon. We started with six nights of LST-locked ON and OFF Moon observations at 40 kHz fine channel resolution and generated difference images of the Moon between $\approx 70 - 180$ MHz. We observed that the individual observations around the FM band were highly contaminated by the Earthshine, which otherwise gets suppressed at coarse channels. We assumed two Earthshine components (the diffuse disk and quasi-specular) in the Moon's emission (McKinley et al. 2018) and used the relation between the specular and diffuse components from

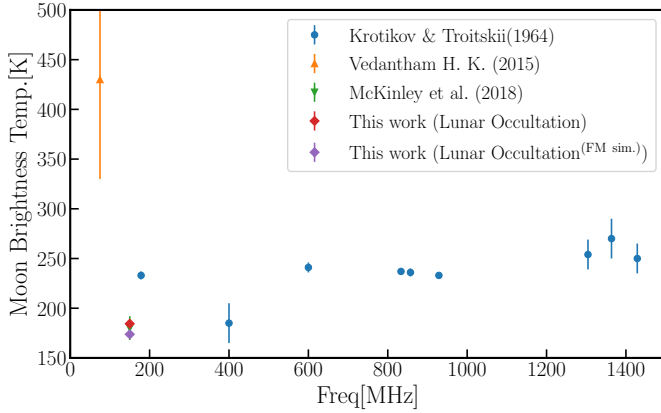


Figure 11. Measurement of the T_{Moon} from our analysis along with the McKinley et al. (2018) result and Table 2 from Krotikov and Troitskii (1964). The values of T_{Moon} from this work are presented as points at 150 MHz.

Evans (1969) to estimate the flux density of the Moon. We took two different approaches to get the final estimates of the flux density of the Moon. In the first approach, similar to McKinley et al. (2018), we utilised the data itself to mitigate the Earthshine from the data, whereas, in the second approach, we used FM simulations to mitigate the Earthshine from the data. We used an FM catalogue of radio transmitters across the Earth to estimate the simulated diffuse Earthshine from the disk of the Moon. Using these methods, we estimated the flux density of the Moon (fig. 4 bottom panel) and converted it into the brightness temperature (ref. eq. 1). The brightness temperature is the measure of the difference between the intrinsic temperature of the Moon (T_{Moon}) and the Galactic foreground temperature ($T_{\text{Gal}}(\nu)$). We have assumed that the Moon had a constant temperature over our desirable frequencies; therefore, we fit the observed brightness temperature from eq. 10 with a modified Galactic power-law equation which had an additional factor of constant temperature offset (T_{offset}) (see eq. 11). The offset temperature measured the T_{Moon} . We jointly estimated the $T_{\text{Gal}}(\nu)$, T_{Moon} and spectral index α by combining all of the three observation epochs while putting a restriction on the T_{Moon} . In our joint analysis, we were able to recover the Galactic spectral index (α) of the occulted sky within 5 – 7% level of the GSM2016 estimates. Also, our estimates of the T_{Moon} ($184.40 \pm 2.65\text{K}$ and $173.77 \pm 2.48\text{K}$ for the first and second Earthshine mitigation methods, respectively) provided tighter constraints and are consistent with the previous results from McKinley et al. (2018).

This shows that we can include multiple nights of data and can strengthen the total SNR of our analysis. The next step would be to check the performance of the foreground subtraction techniques on the data. The estimation of the global 21-cm signal is the ultimate goal of our work. Tackling the prior difficulties of these approaches can put us one step closer to understanding the CD-EoR.

Acknowledgement

This project is supported by an ARC Future Fellowship under grant FT180100321. This research was partially supported by the Australian Research Council Centre of Excellence for All Sky Astrophysics in 3 Dimensions (ASTRO 3D), through project number CE170100013. The International Centre for Radio Astronomy Research (ICRAR) is a Joint Venture of Curtin University and The University of Western Australia, funded by the Western Australian State government. The MWA Phase II upgrade project was supported by Australian Research Council LIEF grant LE160100031 and the Dunlap Institute for Astronomy and Astrophysics at the University of Toronto. This scientific work makes use of Inyarrimanha Ilgari Bundara, the CSIRO Murchison Radio-astronomy Observatory. We acknowledge the Wajarri Yamatji people as the traditional owners and native title holders of the Observatory site. Support for the operation of the MWA is provided by the Australian Government (NCRIS), under a contract to Curtin University administered by Astronomy Australia Limited. We acknowledge the Pawsey Supercomputing Centre, which is supported by the Western Australian and Australian Governments. Data were processed at the Pawsey Supercomputing Centre.

9. Data Availability

The data used in this work will be made available upon reasonable request.

References

- Abdurashidova, Zara, et al. 2021. First Results from HERA Phase I: Upper Limits on the Epoch of Reionization 21 cm Power Spectrum (August). arXiv: 2108.02263 [astro-ph.CO].
- Aghanim, N., et al. 2020. Planck 2018 results. VI. Cosmological parameters. [Erratum: Astron.Astrophys. 652, C4 (2021)], Astron. Astrophys. 641:A6. <https://doi.org/10.1051/0004-6361/201833910>. arXiv: 1807.06209 [astro-ph.CO].
- Barnett, R., S. J. Warren, G. D. Becker, D. J. Mortlock, P. C. Hewett, R. G. McMahon, C. Simpson, and B. P. Venemans. 2017. Observations of the Lyman series forest towards the redshift 7.1 quasar ULAS J1120+0641. Astron. Astrophys. 601:A16. <https://doi.org/10.1051/0004-6361/201630258>. arXiv: 1702.03687 [astro-ph.CO].
- Bernardi, G., J. T. L. Zwart, D. Price, L. J. Greenhill, A. Mesinger, J. Dowell, T. Eftekhari, S. W. Ellingson, J. Kocz, and F. Schinzel. 2016. Bayesian constraints on the global 21-cm signal from the Cosmic Dawn. mnras 461, no. 3 (June): 2847–2855. ISSN: 0035-8711. <https://doi.org/10.1093/mnras/stw1499>. eprint: <https://academic.oup.com/mnras/article-pdf/461/3/2847/8110190/stw1499.pdf>. <https://doi.org/10.1093/mnras/stw1499>.
- Bharadwaj, Somnath, and SK. Saiyad Ali. 2005. On using visibility correlations to probe the HI distribution from the dark ages to the present epoch. 1. Formalism and the expected signal. mnras 356:1519. <https://doi.org/10.1111/j.1365-2966.2004.08604.x>. arXiv: astro-ph/0406676.
- Bowman, Judd D., and Alan E. E. Rogers. 2010. nat 468, no. 7325 (July): 796–798. <https://doi.org/10.1038/nature09601>. <https://doi.org/10.1038%2Fnature09601>.
- Bowman, Judd D., Alan E. E. Rogers, and Jacqueline N. Hewitt. 2008. Toward Empirical Constraints on the Global Redshifted 21 cm Brightness Temperature During the Epoch of Reionization. apj 676, no. 1 (March): 1–9. <https://doi.org/10.1086/528675>. arXiv: 0710.2541 [astro-ph].

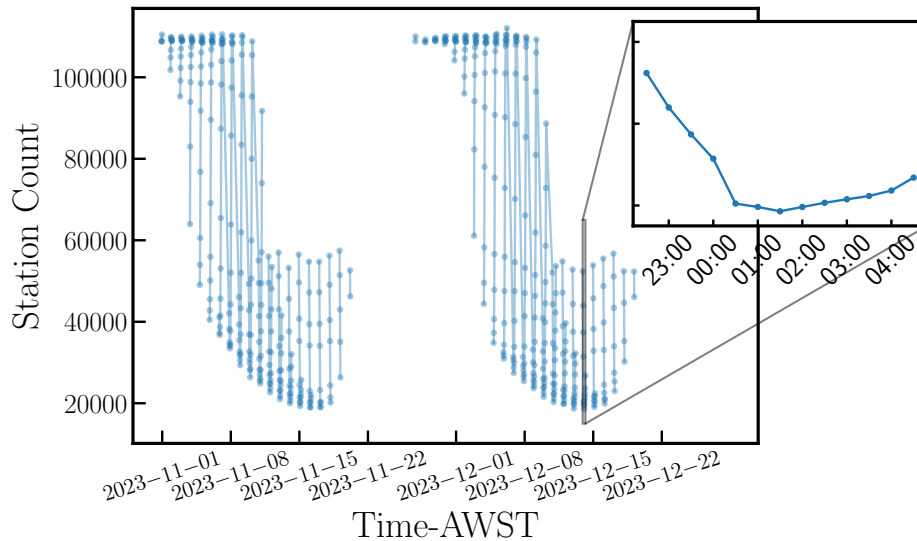


Figure 12. Simulation of the station counts between November and December 2023. The variation of station counts roughly repeats over a month. The individual spikes in the plot correspond to a single night's observation between 20:00-4:30 hrs, with a time separation of 30 mins. The zoomed figure on the top right shows the variation of station counts over a single night from 13th December 2023.

- Bowman, Judd D., Alan E. E. Rogers, Raul A. Monsalve, Thomas J. Mozdzen, and Nivedita Mahesh. 2018. An absorption profile centred at 78 megahertz in the sky-averaged spectrum. *nat* 555 (7694): 67–70. <https://doi.org/10.1038/nature25792>. arXiv: 1810.05912 [astro-ph.CO].
- Burns, Jack O., Stuart Bale, and Richard F. Bradley. 2019. Dark Cosmology: Investigating Dark Matter and Exotic Physics using the Redshifted 21-cm Global Signal with the Dark Ages Polarimeter Pathfinder (DAPPER). In *American astronomical society meeting abstracts #234*, 234:212.02. American Astronomical Society Meeting Abstracts. June.
- Carson, J.R. 1922. Notes on the theory of modulation. *procire* 10 (1): 57–64. <https://doi.org/10.1109/JRPROC.1922.219793>.
- de Oliveira-Costa, Angelica, Max Tegmark, B. M. Gaensler, Justin Jonas, T. L. Landecker, and Patricia Reich. 2008. A model of diffuse Galactic radio emission from 10 MHz to 100 GHz. *mnras* 388, no. 1 (July): 247–260. <https://doi.org/10.1111/j.1365-2966.2008.13376.x>. arXiv: 0802.1525 [astro-ph].
- DeBoer, David R., et al. 2017. Hydrogen Epoch of Reionization Array (HERA). *Publ. Astron. Soc. Pac.* 129 (974): 045001. <https://doi.org/10.1088/1538-3873/129/974/045001>. arXiv: 1606.07473 [astro-ph.IM].
- Dowell, Jayce, Gregory B. Taylor, Frank K. Schinzel, Namir E. Kassim, and Kevin Stovall. 2017. The LWA1 Low Frequency Sky Survey. *mnras* 469, no. 4 (August): 4537–4550. <https://doi.org/10.1093/mnras/stx1136>. arXiv: 1705.05819 [astro-ph.IM].
- Eastwood, Michael W., Marin M. Anderson, Ryan M. Monroe, Gregg Hallinan, Morgan Catha, Jayce Dowell, Hugh Garsden, et al. 2019. The 21 cm power spectrum from the cosmic dawn: first results from the OVRO-LWA. *AJ* 158, no. 2 (July): 84. <https://doi.org/10.3847/1538-3881/ab2629>. <https://doi.org/10.3847/1538-3881/ab2629>.
- Evans, J. V. 1969. Radar studies of planetary surfaces. *ARAnA* 7 (1): 201–248. <https://doi.org/10.1146/annurev.aa.07.090169.001221>.
- Evans, John V., and Tor Hagfors. 1966. Study of radio echoes from the moon at 23 centimeters wavelength. *Journal of Geophysical Research* 71:4871–4889. <https://api.semanticscholar.org/CorpusID:129777556>.
- Fan, Xiaohui, et al. 2003. A Survey of $z > 5.7$ quasars in the Sloan Digital Sky Survey. 2. Discovery of three additional quasars at $z > 6$. *Astron. J.* 125:1649. <https://doi.org/10.1086/368246>. arXiv: astro-ph/0301135.
- Furlanetto, Steven, S. Peng Oh, and Frank Briggs. 2006. Cosmology at Low Frequencies: The 21 cm Transition and the High-Redshift Universe. *Phys. Rept.* 433:181–301. <https://doi.org/10.1016/j.physrep.2006.08.002>. arXiv: astro-ph/0608032.
- Furlanetto, Steven R., Aaron Sokasian, and Lars Hernquist. 2004. Observing the reionization epoch through 21-centimetre radiation. *mnras* 347, no. 1 (January): 187–195. issn: 0035-8711. <https://doi.org/10.1111/j.1365-2966.2004.07187.x>.
- Haykin, Simon. 1989. *An intro to analog and digital communications*. xvi, 652 p. Wiley New York. Book. <https://nla.gov.au/nla.cat-vn431517>.
- Hogan, C. J., and M. J. Rees. 1979. Spectral appearance of non-uniform gas at high z . *mnras* 188 (September): 791–798. <https://doi.org/10.1093/mnras/188.4.791>.
- Jordan, C. H., S. Murray, C. M. Trott, R. B. Wayth, D. A. Mitchell, M. Rahimi, B. Pindor, P. Procopio, and J. Morgan. 2017. Characterization of the ionosphere above the Murchison Radio Observatory using the Murchison Widefield Array. *mnras* 471, no. 4 (July): 3974–3987. issn: 0035-8711. <https://doi.org/10.1093/mnras/stx1797>. <https://doi.org/10.1093/mnras/stx1797>.
- Komatsu, E., et al. 2011. Seven-Year Wilkinson Microwave Anisotropy Probe (WMAP) Observations: Cosmological Interpretation. *ApJS* 192:18. <https://doi.org/10.1088/0067-0049/192/2/18>. arXiv: 1001.4538 [astro-ph.CO].
- Krotikov, V D, and V S Troitskii. 1964. Radio emission and nature of the moon. *Soviet Physics Uspekhi* 6, no. 6 (June): 841. <https://doi.org/10.1070/PU1964v006n06ABEH003615>. <https://dx.doi.org/10.1070/PU1964v006n06ABEH003615>.
- Line, J. L. B., R. L. Webster, B. Pindor, D. A. Mitchell, and C. M. Trott. 2017. Puma: the positional update and matching algorithm. *pasa* 34:e003. <https://doi.org/10.1017/pasa.2016.58>.
- Makinen, T. Lucas, Lachlan Lancaster, Francisco Villaescusa-Navarro, Peter Melchior, Shirley Ho, Laurence Perreault-Levasseur, and David N. Spergel. 2021. deep21: a deep learning method for 21 cm foreground removal. *jcip* 2021, no. 4 (April): 081. <https://doi.org/10.1088/1475-7516/2021/04/081>. arXiv: 2010.15843 [astro-ph.CO].

- Mather, J. C., E. S. Cheng, D. A. Cottingham, Jr. Eplee R. E., D. J. Fixsen, T. Hewagama, R. B. Isaacman, et al. 1994. Measurement of the Cosmic Microwave Background Spectrum by the COBE FIRAS Instrument. *apj* 420 (January): 439. <https://doi.org/10.1086/173574>.
- McKinley, B, G Bernardi, C M Trott, J L B Line, R B Wayth, A R Offringa, B Pindor, et al. 2018. Measuring the global 21-cm signal with the MWA-I: improved measurements of the Galactic synchrotron background using lunar occultation. *mnras* 481, no. 4 (September): 5034–5045. issn: 0035-8711. <https://doi.org/10.1093/mnras/sty2437>. <https://doi.org/10.1093/mnras/sty2437>.
- McKinley, B, F. Briggs, D. L. Kaplan, L. J. Greenhill, G. Bernardi, J. D. Bowman, A. de Oliveira-Costa, et al. 2012. Low-frequency observations of the moon with the murchison widefield array. *AJ* 145, no. 1 (December): 23. issn: 1538-3881. <https://doi.org/10.1088/0004-6256/145/1/23>. <http://dx.doi.org/10.1088/0004-6256/145/1/23>.
- McQuinn, Matthew, Oliver Zahn, Matias Zaldarriaga, Lars Hernquist, and Steven R. Furlanetto. 2006. Cosmological parameter estimation using 21 cm radiation from the epoch of reionization. *ApJ* 653:815–830. <https://doi.org/10.1086/505167>. arXiv: astro-ph/0512263.
- Mertens, F. G., et al. 2020. Improved upper limits on the 21-cm signal power spectrum of neutral hydrogen at $z \sim 9.1$ from LOFAR. *mnras* 493 (2): 1662–1685. <https://doi.org/10.1093/mnras/staa327>. arXiv: 2002.07196 [astro-ph.CO].
- Mertens, F. G., B. Semelin, and L. V. E. Koopmans. 2021. Exploring the Cosmic Dawn with NenuFAR, edited by A. Siebert, K. Baillié, E. Lagadec, N. Lagarde, J. Malzac, J. -B. Marquette, M. N'Diaye, J. Richard, and O. Venot, 211–214. December. <https://doi.org/10.48550/arXiv.2109.10055>. arXiv: 2109.10055 [astro-ph.CO].
- Mesinger, Andrei, ed. 2016. Understanding the Epoch of Cosmic Reionization. Vol. 423. Astrophysics and Space Science Library. January. <https://doi.org/10.1007/978-3-319-21957-8>.
- Monsalve, Raul A., Alan E. E. Rogers, Judd D. Bowman, and Thomas J. Mozdzen. 2017. CALIBRATION OF THE EDGES HIGH-BAND RECEIVER TO OBSERVE THE GLOBAL 21 cm SIGNATURE FROM THE EPOCH OF REIONIZATION. *ApJ* 835, no. 1 (January): 49. <https://doi.org/10.3847/1538-4357/835/1/49>. <https://doi.org/10.3847/1538-4357/835/1/49>.
- Offringa, A. R., B. McKinley, Hurley-Walker, et al. 2014. WSClean: an implementation of a fast, generic wide-field imager for radio astronomy. *mnras* 444 (1): 606–619. <https://doi.org/10.1093/mnras/stu1368>.
- Offringa, A. R., R. B. Wayth, N. Hurley-Walker, D. L. Kaplan, N. Barry, A. P. Beardley, M. E. Bell, et al. 2015. The low-frequency environment of the murchison widefield array: radio-frequency interference analysis and mitigation. *pasa* 32. <https://doi.org/10.1017/pasa.2015.7>.
- Paciga, Gregory, et al. 2013. A refined foreground-corrected limit on the HI power spectrum at $z=8.6$ from the GMRT Epoch of Reionization Experiment. *mnras* 433:639. <https://doi.org/10.1093/mnras/stt753>. arXiv: 1301.5906 [astro-ph.CO].
- Paciga, Gregory, Tzu-Ching Chang, Yashwant Gupta, Rajaram Nityanada, Julia Odegova, Ue-Li Pen, Jeffrey Peterson, Jayanta Roy, and Kris Sigurdson. 2011. The GMRT Epoch of Reionization experiment: A New upper limit on the neutral hydrogen power spectrum at $z \sim 8.6$. *mnras* 413:1174–1183. <https://doi.org/10.1111/j.1365-2966.2011.18208.x>. arXiv: 1006.1351 [astro-ph.CO].
- Parsons, Aaron R., et al. 2014. New Limits on 21cm EoR From PAPER-32 Consistent with an X-Ray Heated IGM at $z=7.7$. *ApJ* 788:106. <http://doi.org/10.1088/0004-637X/788/2/106>. arXiv: 1304.4991 [astro-ph.CO].
- Patra, Nipanjana, Ravi Subrahmanyan, Agaram Raghunathan, and Udaya Narayana Rao. 2012. Saras: a precision system for measurement of the cosmic radio background and signatures from the epoch of reionization. *Experimental Astronomy* 36 (November). <https://doi.org/10.1007/s10686-013-9336-3>.
- Philip, L., Z. Abdurashidova, H. C. Chiang, N. Ghazi, A. Gumba, H. M. Heilgendorff, J. M. Jauregui-Garcia, et al. 2019. Probing radio intensity at high- z from marion: 2017 instrument. *JoAI* 08 (02): 1950004. <https://doi.org/10.1142/S2251171719500041>. eprint: <https://doi.org/10.1142/S2251171719500041>. <https://doi.org/10.1142/S2251171719500041>.
- Pober, Jonathan, A. Parsons, D. Backer, R. Bradley, C. Parashare, N. Gugliucci, E. Benoit, et al. 2011. The Precision Array for Probing the Epoch of Reionization. In *American astronomical society meeting abstracts* 217, 217:432.06. American Astronomical Society Meeting Abstracts. January.
- Pritchard, Jonathan R., and Abraham Loeb. 2012. 21-cm cosmology. *rpp* 75:086901. <https://doi.org/10.1088/0034-4885/75/8/086901>. arXiv: 1109.6012 [astro-ph.CO].
- Remazeilles, M., C. Dickinson, A. J. Banday, M. -A. Bigot-Sazy, and T. Ghosh. 2015. An improved source-subtracted and destripped 408-MHz all-sky map. *mnras* 451, no. 4 (August): 4311–4327. <https://doi.org/10.1093/mnras/stv1274>. arXiv: 1411.3628 [astro-ph.IM].
- Shaver, P. A., R. A. Windhorst, P. Madau, and A. G. de Bruyn. 1999. Can the reionization epoch be detected as a global signature in the cosmic background? *aap* 345 (May): 380–390. arXiv: astro-ph/9901320 [astro-ph].
- Sigel, D. A., V. M. Bach, M. W. Thomson, Richard F. Bradley, L. R. Amaro, J. Lazio, and J. O. Burns. 2013. Deployable antenna concepts for the dark ages radio explorer mission, 1–1. <https://doi.org/10.1109/USNC-URSI-NRSM.2013.6525025>.
- Singh, Saurabh, Nambissan T. Jishnu, Ravi Subrahmanyan, N. Udaya Shankar, B. S. Girish, A. Raghunathan, R. Somashekar, K. S. Srivani, and Mayuri Sathyanarayana Rao. 2022. On the detection of a cosmic dawn signal in the radio background. *nat* 6 (February): 607–617. <https://doi.org/10.1038/s41550-022-01610-5>. arXiv: 2112.06778 [astro-ph.CO].
- Singh, Saurabh, Ravi Subrahmanyan, N. Udaya Shankar, Mayuri Sathyanarayana Rao, Anastasia Fialkov, Aviad Cohen, Rennan Barkana, et al. 2017. First results on the epoch of reionization from first light with SARAS 2. *ApJ* 845, no. 2 (August): L12. <https://doi.org/10.3847/2041-8213/aa831b>. <https://doi.org/10.3847/2041-8213/aa831b>.
- Singh, Saurabh, Ravi Subrahmanyan, N. Udaya Shankar, Mayuri Sathyanarayana Rao, Anastasia Fialkov, Aviad Cohen, Rennan Barkana, et al. 2018. SARAS 2 Constraints on Global 21 cm Signals from the Epoch of Reionization. *apj* 858, no. 1 (May): 54. <https://doi.org/10.3847/1538-4357/aabae1>. arXiv: 1711.11281 [astro-ph.CO].
- Sokolowski, Marcin, Steven E. Tremblay, Randall B. Wayth, Steven J. Tingay, Nathan Clarke, Paul Roberts, Mark Waterson, et al. 2015. BIGHORNS - Broadband Instrument for Global HydrOgen ReioNisation Signal. *pasa* 32 (February): e004. <https://doi.org/10.1017/pasa.2015.3>. arXiv: 1501.02922 [astro-ph.IM].
- Tauscher, Keith, David Rapetti, Bang D. Nhan, Alec Handy, Neil Bassett, Joshua Hibbard, David Bordenave, Richard F. Bradley, and Jack O. Burns. 2021. Global 21 cm signal extraction from foreground and instrumental effects. IV. accounting for realistic instrument uncertainties and their overlap with foreground and signal models. *The Astrophysical Journal* 915, no. 1 (July): 66. <https://doi.org/10.3847/1538-4357/ac00af>. <https://doi.org/10.3847/1538-4357/ac00af>.
- Tingay, S. J., R. Goeke, J. D. Bowman, D. Emrich, S. M. Ord, D. A. Mitchell, M. F. Morales, et al. 2013. The murchison widefield array: the square kilometre array precursor at low radio frequencies. *pasa* 30. issn: 1448-6083. <https://doi.org/10.1017/pasa.2012.007>. <http://dx.doi.org/10.1017/pasa.2012.007>.
- Trott, Cathryn M. 2014. Comparison of Observing Modes for Statistical Estimation of the 21 cm Signal from the Epoch of Reionisation. *pasa* 31 (July): e026. <https://doi.org/10.1017/pasa.2014.23>. arXiv: 1405.0357 [astro-ph.CO].

- Trott, Cathryn M., et al. 2020. Deep multiredshift limits on Epoch of Reionization 21 cm power spectra from four seasons of Murchison Widefield Array observations. *mnras* 493 (4): 4711–4727. <https://doi.org/10.1093/mnras/staa414>. arXiv: 2002.02575 [astro-ph.CO].
- Trott, Cathryn M., C. H. Jordan, S. G. Murray, B. Pindor, D. A. Mitchell, R. B. Wayth, J. Line, et al. 2018. Assessment of ionospheric activity tolerances for epoch of reionization science with the murchison widefield array. *ApJ* 867, no. 1 (September): 15. <https://doi.org/10.3847/1538-4357/aae314>. <https://dx.doi.org/10.3847/1538-4357/aae314>.
- van Haarlem and others. 2013. Lofar: the low-frequency array. *AnA* 556:A2. <https://doi.org/10.1051/0004-6361/201220873>. <https://doi.org/10.1051/0004-6361/201220873>.
- Vedantham, H. K., L. V. E. Koopmans, A. G. de Bruyn, S. J. Wijnholds, M. Brentjens, F. B. Abdalla, K. M. B. Asad, et al. 2015. Lunar occultation of the diffuse radio sky: lofar measurements between 35 and 80 mhz. *mnras* 450, no. 3 (May): 2291–2305. ISSN: 1365-2966. <https://doi.org/10.1093/mnras/stv746>. <http://dx.doi.org/10.1093/mnras/stv746>.
- Voytek, Tabitha C., Aravind Natarajan, Jose Miguel Jauregui Garcia, Jeffrey B. Peterson, and Omar Lopez-Cruz. 2014. *ApJ* 782, no. 1 (January): L9. <https://doi.org/10.1088/2041-8205/782/1/L9>.
- Wayth, Randall, Marcin Sokolowski, Tom Booler, Brian Crosse, David Emrich, Robert Grootjans, Peter J. Hall, et al. 2017. *pasa*, e034. <https://doi.org/10.1017/pasa.2017.27>.
- Zheng, H., M. Tegmark, J. S. Dillon, D. A. Kim, A. Liu, A. R. Neben, J. Jonas, P. Reich, and W. Reich. 2017. An improved model of diffuse galactic radio emission from 10 MHz to 5 THz. *mnras* 464, no. 3 (January): 3486–3497. <https://doi.org/10.1093/mnras/stw2525>. arXiv: 1605.04920 [astro-ph.CO].
- Zuo, Shifan, Xuelei Chen, Reza Ansari, and Youjun Lu. 2019. 21 cm Signal Recovery via Robust Principal Component Analysis. *aj* 157, no. 1 (January): 4. <https://doi.org/10.3847/1538-3881/aaef3b>. arXiv: 1801.04082 [astro-ph.CO].

Appendix 1. Noise Estimation

Appendix 1.1 For $S_m(\nu)$

Our analysis used 34 full-band observations (72–230 MHz), with each full-band observation comprising 5 coarse-band observations (in the context of MWA, each coarse-band observation is at 1.28 MHz resolution and 30.72 MHz wide). We produced the beam-corrected images at every 40 kHz fine channel for each of the observations. As a result, we had 768×5 beam-corrected images for each full-band observation. We evaluated the RMS noise for both disk and quasi-specular components ($\Delta S_{\text{disk}}, \Delta S_{\text{spec}}$) using eq.4 and propagated these errors through eq.6 to estimate $\Delta S_m(\nu)$. In eq. 6, we used the values of $S_{\text{disk}}(\nu_0)$ to get $S_{\text{diffuse}}(\nu_0)$. We fitted a line to $S_{\text{disk}}(\nu)$ and obtained $S_m(\nu_0)$ as the fitted value at ν_0 .

$$S_{\text{diffuse}}(\nu_0) = S_{\text{disk}}(\nu_0) - Y_{\text{fit}}(\nu_0)$$

The errors on the fitting parameters, namely the slope and intercept ($\Delta m, \Delta c$) of the fitted line, were used to obtain the fitting error of the line at ν_0 .

$$\Delta Y_{\text{fit}}(\nu_0) = \sqrt{(\Delta m \times \nu_0)^2 + \Delta c^2}$$

therefore, $\Delta S_{\text{diffuse}}(\nu_0)$ was evaluated as,

$$\Delta S_{\text{diffuse}}(\nu_0) = \sqrt{\Delta S_{\text{disk}}^2(\nu_0) + \Delta Y_{\text{fit}}^2(\nu_0)}$$

Please note that, as our T-tests satisfy the null hypothesis at ν_0 in all three epochs, we used the same value of uncertainty $\Delta S_{\text{diffuse}}(\nu_0)$ in both methods of Earthshine mitigation. From there, we estimated $\Delta R_e(\nu)$,

$$\Delta R_e(\nu) = \left(\frac{\nu}{\nu_0}\right)^{0.58} \times \sqrt{\left(\frac{\Delta S_{\text{diffuse}}(\nu_0)}{S_{\text{diffuse}}(\nu_0)}\right)^2 + \left(\frac{\Delta S_{\text{spec}}(\nu_0)}{S_{\text{spec}}(\nu_0)}\right)^2} \quad (12)$$

and $\Delta S_{\text{diffuse}}(\nu)$ was obtained using,

$$\Delta S_{\text{diffuse}}(\nu) = R_e(\nu) S_{\text{spec}}(\nu) \times \sqrt{\left(\frac{\Delta R_e(\nu)}{R_e(\nu)}\right)^2 + \left(\frac{\Delta S_{\text{spec}}(\nu)}{S_{\text{spec}}(\nu)}\right)^2} \quad (13)$$

Finally, $\Delta S_m(\nu)$ was estimated as,

$$\Delta S_m(\nu) = \sqrt{\Delta S_{\text{disk}}^2(\nu) + \Delta S_{\text{diffuse}}^2(\nu)} \quad (14)$$

As a final result, we had $S_m(\nu)$ and $\Delta S_m(\nu)$ for all 34 full-band observations and propagated them as quadrature in the mean. We put the estimated errors in eq.1 to estimate the occulted sky temperature and errors therein.

Appendix 1.2 For GSM $T_{\text{Gal}}(\nu)$ and $T_{\text{refl-Gal}}(\nu)$ models

We used GSM models to generate the sky maps in the middle of each 34 full-band observations. The maps were generated to match the observed frequency range with a frequency resolution of 5 MHz. In order to get the Galactic temperature (T_{Gal150}) and Galactic spectral index (α), we fit our model with a power-law equation

$$T_{\text{Gal}}(\nu) = T_{\text{Gal150}} \left(\frac{\nu}{150\text{MHz}}\right)^\alpha \quad (15)$$

We used the GSM2016 model to represent the Galactic temperature. We used the model's 5% intrinsic map estimation error in the fitting and measured the values of T_{Gal150} and α for all 34 full-band observations. The fitted parameters ($T_{\text{Gal150}}, \alpha$) and the uncertainties on the fitted parameter ($\Delta T_{\text{Gal150}}, \Delta \alpha$) values were propagated in the quadrature rule. In a similar fashion, we estimated the uncertainties in the $T_{\text{refl-Gal}}(\nu)$ using the eq. 9 (to distinguish between the spectral index parameter of the reflected Galactic power-law equation and the Galactic power-law equation, we denoted the reflected spectral index parameter in eq. 9 as β).

Appendix 1.3 Reflected flux density variation with station count

We obtained the reflected FM flux density corresponding to every ON-Moon observation comprising the FM band.

The variation of the reflected FM flux density changes with the number of FM stations. The increasing number of FM stations can be understood as the more terrestrial land area being exposed to the Moon. Fig. 13 showing the variation in the reflected flux density at three-time stamps during the second observing epoch.

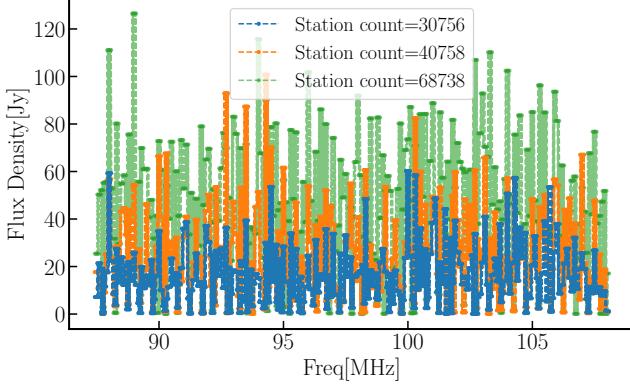


Figure 13. Reflected FM flux density at three different time stamps during the second observing epoch.

Appendix 1.4 T-test results

We estimated the p -values from the T-test at all fine-frequency channels. As we already mentioned the limitation of our simulations, our T-tests performed poorly on more than half of the fine-frequency channels. The null hypothesis got rejected at those channels. However, we only required a single value of S_{diffuse} at ν_0 to estimate $R_c(\nu)$ and since our T-test accepted the null hypothesis at $\approx \nu_0$ at all three epochs, we utilised the values of simulated reflected flux density $S_{\text{FM}}(\nu_0)$ as $S_{\text{diffuse}}(\nu_0)$. Fig. 14 showing the T-test results on the dataset from the first epoch.

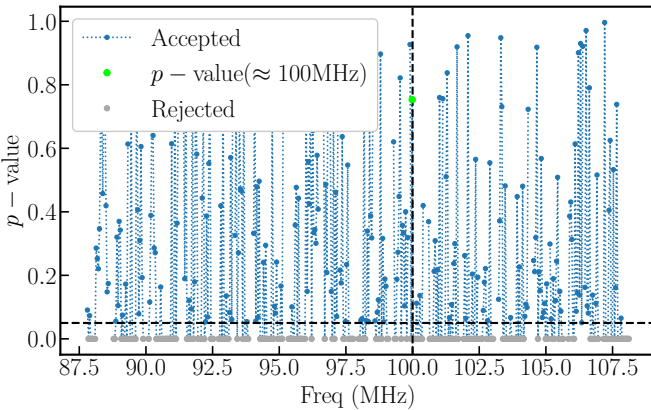


Figure 14. T-test results on the first epoch datasets. X-axis shows the FM frequency band, and the Y-axis shows the corresponding p -values. The horizontal line is at $p = 0.05$, above which the null hypothesis is considered to be accepted. The data points shown in blue colour show the accepted, and the grey colour show rejected frequency channels. The p -value at $\approx \nu_0$ is shown with lime colour.

Appendix 1.5 Correlation between the fitted parameters

Table 5. Correlation between the parameters of eq. 11 when fitted with the dataset from the first epoch using the first Earthshine mitigation method.

	T_{Gal150}	α	T_{offset}
T_{Gal150}	1	0.99	0.99
α	.	1	0.99
T_{offset}	.	.	1

Our final estimates of occulted sky temperature T_{Gal150} , Galactic spectral index α , and offset temperature T_{offset} (which represents the T_{Moon}) show a very high correlation with each other. When checked on the single night dataset (from fig. 8), it showed a near unity level of correlation, see table 5.

The sky position of the Moon is different at all three observing epochs; hence, the galactic spectral index and occulted sky temperature are also different at all three epochs. In the joint analysis, we considered these parameters as independent parameters while restricting T_{offset} (assuming the Moon to have the same temperature across the epochs). The correlation table (6) between all parameters still shows a high correlation, however, the spectral index shows less correlation compared to the temperature parameters.

Table 6. The correlation between the parameter of eq. 11 when fitted jointly with combined datasets from all three epochs.

	$T_{\text{Gal150; Aug.}}$	$T_{\text{Gal150; Sept.}}$	$T_{\text{Gal150; Dec.}}$	$\alpha_{\text{fitting; Aug.}}$	$\alpha_{\text{fitting; Sept.}}$	$\alpha_{\text{fitting; Dec.}}$	T_{offset}
$T_{\text{Gal150; Aug.}}$	1.000	0.965	0.954	0.914	0.797	0.806	0.992
$T_{\text{Gal150; Sept.}}$.	1.000	0.932	0.911	0.819	0.790	0.973
$T_{\text{Gal150; Dec.}}$.	.	1.000	0.897	0.770	0.848	0.958
$\alpha_{\text{fitting; Aug.}}$.	.	.	1.000	0.753	0.761	0.936
$\alpha_{\text{fitting; Sept.}}$	1.000	0.653	0.804
$\alpha_{\text{fitting; Dec.}}$	1.000	0.812
T_{offset}	1.000

Table 7. Table showing the best-fit parameters from all sky models for every individual case.

Epoch	Sky – model	$T_{\{\text{Gal150; model}\}} \text{ (K)}$	α_{model}	Fitting	$T_{\{\text{Gal150; fitting}\}} \text{ (K)}$	α_{fitting}	$T_{\{\text{Moon}\}} \text{ (K)}$
Aug.	GSM	250.4 ± 12.5	-2.540 ± 0.002	Method 1	199.2 ± 5.4	-2.70 ± 0.05	188.3 ± 4.6
				Method 2 (FM sim.)	183.5 ± 5.1	-2.79 ± 0.05	174.2 ± 4.4
	GSM2016	242.7 ± 12.1	-2.621 ± 0.003	.	195.5 ± 5.3	-2.72 ± 0.05	186.1 ± 4.5
				..	179.2 ± 5.0	-2.82 ± 0.05	171.4 ± 4.3
	LFSM	313.9 ± 15.7	-2.689 ± 0.003	.	202.8 ± 5.3	-2.70 ± 0.05	188.5 ± 4.5
				..	189.0 ± 5.1	-2.78 ± 0.05	176.2 ± 4.4
Haslam	253.7 ± 12.7	-2.603 ± 0.003	.	199.2 ± 5.3	-2.71 ± 0.05	187.9 ± 4.6	
			..	183.7 ± 5.1	-2.80 ± 0.05	174.0 ± 4.3	
Sept.	GSM	253.4 ± 12.7	-2.540 ± 0.002	.	177.6 ± 4.4	-2.54 ± 0.04	189.4 ± 4.2
				..	185.6 ± 5.1	-2.43 ± 0.05	198.5 ± 4.9
	GSM2016	241.0 ± 12.0	-2.585 ± 0.003	.	174.4 ± 4.3	-2.56 ± 0.04	187.4 ± 4.4
				..	182.2 ± 5.0	-2.47 ± 0.05	196.0 ± 4.8
	LFSM	295.3 ± 14.8	-2.689 ± 0.003	.	180.8 ± 4.4	-2.56 ± 0.04	189.2 ± 4.2
				..	188.6 ± 5.0	-2.46 ± 0.04	198.0 ± 4.8
Haslam	250.7 ± 12.5	-2.603 ± 0.003	.	177.4 ± 4.4	-2.56 ± 0.04	188.9 ± 4.2	
			..	185.2 ± 5.0	-2.45 ± 0.05	197.8 ± 4.8	
Dec.	GSM	395.8 ± 19.8	-2.496 ± 0.002	.	235.6 ± 5.4	-2.66 ± 0.04	173.8 ± 5.0
				..	239.5 ± 4.1	-2.60 ± 0.03	177.4 ± 3.8
	GSM2016	380.4 ± 19.0	-2.497 ± 0.003	.	232.1 ± 5.4	-2.68 ± 0.04	172.2 ± 5.0
				..	235.7 ± 4.0	-2.62 ± 0.03	175.5 ± 3.7
	LFSM	453.4 ± 22.7	-2.557 ± 0.003	.	238.7 ± 5.4	-2.68 ± 0.04	173.7 ± 5.0
				..	242.4 ± 4.0	-2.62 ± 0.03	177.2 ± 3.7
Haslam	414.2 ± 20.6	-2.603 ± 0.003	.	236.0 ± 5.4	-2.68 ± 0.04	173.4 ± 5.0	
			..	239.7 ± 4.0	-2.62 ± 0.03	176.8 ± 3.7	

Table 8. Left: Joint-fit estimates of T_{Moon} from all sky models. Right: GSM2016 model fit estimates for removed FM-band.

Sky – model	$T_{\{\text{Moon}\}} \text{ (K)}$	Fitting	Epoch	$T_{\{\text{Gal150}\}} \text{ (K)}$	$T_{\{\text{Moon}\}} \text{ (K)}$	Joint Fitting	
GSM	186.5 ± 2.7	Method 1	Aug.	196.9 ± 6.1	187.6 ± 5.3	Method 1	
				176.7 ± 2.5	179.5 ± 5.6	171.3 ± 4.8	Method 2 (FM sim.)
GSM2016	184.4 ± 2.6	Method 2 (FM sim.)	Sept.	174.8 ± 4.8	187.7 ± 4.6	.	
				173.8 ± 2.5	181.3 ± 4.9	195.1 ± 4.7	..
LFSM	186.6 ± 2.7	.	Dec.	223.3 ± 5.3	164.5 ± 4.9	.	
				178.7 ± 2.5	236.2 ± 4.3	175.9 ± 4.0	..
Haslam	186.1 ± 2.7	..	Joint Aug.	192.6 ± 3.4	184.5 ± 2.9	Method 1	
				177.2 ± 3.7	171.5 ± 3.2	"	.
Haslam	176.4 ± 2.5	..	Sept.	243.2 ± 3.3	"	.	
				177.2 ± 3.7	243.2 ± 3.3	"	.
Haslam	176.4 ± 2.5	..	Dec.	Joint Aug.	178.8 ± 3.0	173.3 ± 2.6	Method 2 (FM sim.)
				176.4 ± 2.5	159.1 ± 2.8	"	..
				Dec.	231.5 ± 2.9	"	..